TROPICAL OCEANIC PRECIPITATION FREQUENCY FROM NIMBUS 5 MICROWAVE DATA

by Stanley Q. Kidder

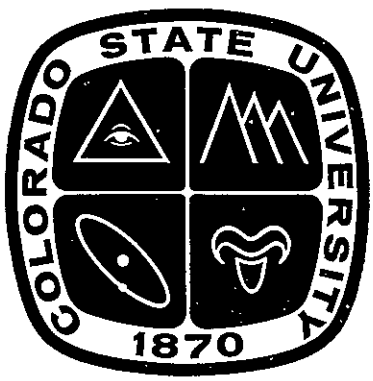

Atmospheric Science
PAPER NO.
248

DEPARTMENT OF ATMOSPHERIC SCIENCE
COLORADO STATE UNIVERSITY
FORT COLLINS, COLORADO

US ISSN 0067-0340

ABSTRACT

Microwave brightness temperature data from the Nimbus 5 satellite have been analyzed, using threshold brightness temperatures, to yield tropical oceanic precipitation frequencies for several classes of rainfall rates during the season December 1972 through February 1973. Data taken near local noon and near local midnight were analyzed. The overall results are consistent with both climatological precipitation frequency and with concurrent satellite-derived frequency of highly reflective clouds. The difference between the local noon and local midnight frequencies is small, but the heavier rainfall rates tend to occur more frequently near local noon. The ratios of the frequencies of light, moderate, and heavy rain were observed to be relatively constant over the tropical oceans. Passive microwave measurements from space seem to be an important step toward accurate measurement of oceanic precipitation.

ACKNOWLEDGEMENTS

The author wishes to thank his advisor, Dr. Thomas H. Vonder Haar, whose advise and encouragement made this paper possible; Dr. Wayne H. Schubert, Dr. David A. Kruger, and Mr. James S. Ellis for their critical review of the manuscript; Ms. Charline Polifka for her invaluable computer programming assistance, Mr. Mark Howes for his drafting of the figures; and Ms. Pamela Brubacher for typing the manuscript. This research was sponsored by the National Aeronautics and Space Administration under Grant NGR-06-002-102. Acknowledgment is also made to the National Center for Atmospheric Research, which is sponsored by the National Science Foundation, for the computing time used in this research.

TABLE OF CONTENTS

LIST OF FIGURES

Figures (cont.) Page

LIST OF TABLES

1.0 INTRODUCTION

Knowledge of oceanic precipitation is of fundamental importance to meteorology. Approximately 80% of the earth's precipitation falls in the ocean (Sellers, 1965) where fewer than ten percent of the world's weather stations exist. Yet the latent heat released over the ocean plays a major role in the maintenance of the general circulation and effects almost everything known as "weather".

Many ingenious attempts have been made to determine oceanic precipitation amounts, but all are indirect methods which are only remotely connected with areal precipitation. Many of these efforts rely on extrapolations of island and coastal data (c. f. Jacobs, 1968) which constitute an extremely small sample over the approximately 3.5×10^8 km^2 of ocean. Ships' logs have been used to compile climatological means of such meteorological parameters as wind, cloudiness, precipitation frequency (McDonald, 1938), and even precipitation amounts from qualitative weather (WW) codes (Tucker, 1961). Shipping lanes are such, however, that many data are taken at certain times and places while few are taken elsewhere. More recently satellite data, which is free of many kinds of sampling bias, have been used to estimate precipitation. Until the launch of Cosmos 243 in 1968 and Nimbus 5 in 1972, however, all of the data were from the visible or infrared portions of the electromagnetic spectrum in which precipitation cannot be observed directly due to the opacity of clouds.*

---

*See Martin and Scherer (1973) and Dittberner and Vonder Haar (1973) for a review of precipitation estimation techniques using visible and infrared satellite data.

A solution to the problem of the determination of oceanic precipitation seems to be passive microwave sensing from satellites. Raindrops, being strong emitters and scatterers of microwave radiation, can be detected at satellite altitudes over the ocean even through clouds, which are practically transparent in the microwave region. In this paper, data from the Electrically Scanning Microwave Radiometer (ESMR) aboard Nimbus 5 are used to determine precipitation frequency over the ocean during one season. This is a first step toward measuring latent heat release over oceans, and the results may be directly used to test the operation of numerical models of the general circulation (c. f. Holloway and Manabe, 1971).

2.0 THE TRANSFER OF MICROWAVE RADIATION

2.1 Radiative Transfer Theory

The equation of radiative transfer may be written (Chandrasekhar, 1960):

$$\frac{dN_\lambda(\vec{r},\vec{s})}{dz} = -(\alpha_s+\alpha_a)N_\lambda(\vec{r},\vec{s})+\alpha_a B_\lambda(T)+\alpha_s \int_0^{4\pi} P(\vec{r},\vec{s},\vec{s}')N_\lambda(\vec{r},\vec{s}')d\Omega_{s'} \qquad (1)$$

where $N_\lambda(\vec{r},\vec{s})$ is the spectral radiance (power per unit wavelength per steradian per unit area perpendicular to $\vec{s}$) at the point $\vec{r}$ in the direction $\vec{s}$, $B_\lambda(T)$ is the Planck function, α_s and α_a are the volume scattering and absorption coefficients, respectively, $P(\vec{r},\vec{s},\vec{s}')$ is the scattering phase function, and z is the distance along the ray path. Qualitatively, equation (1) gives the rate of change of the radiance along the path at point $\vec{r}$ in terms of 1) the radiance absorbed and scattered out of the beam by the medium, 2) the radiance added to the beam by thermal emission of the medium, and 3) radiance scattered into the beam from other directions. In the microwave region (λ>1 mm), N_λ is proportional to equivalent blackbody (or brightness) temperature, T_B, and the Planck function is proportional to local temperature by the Rayleigh-Jeans Law. Therefore, equation (1) becomes

$$\frac{dT_B(\vec{r},\vec{s})}{dz} = -(\alpha_s+\alpha_a)T_B(\vec{r},\vec{s}) + \alpha_a T(\vec{r}) + \alpha_s S_c \qquad (2)$$

where

$$S_c \equiv \int_0^{4\pi} P(\vec{r},\vec{s},\vec{s}')T_B(\vec{r},\vec{s}')d\Omega_{s'} \qquad (3)$$

The brightness temperature measured by a satellite-borne radiometer can be obtained by integrating the first order, linear differential equation (2) from the surface to the top of the atmosphere H

$$T_B(\theta) = T_{BO}(\theta)t_{O,H}(\theta) + \int_0^H t_{Z,H}(\theta)\left[\alpha_a T+\alpha_s S_c\right] dZ \tag{4}$$

The factor t is the fractional transmittance through a certain layer,

$$t_{a,b} \equiv e^{-\tau_{a,b}} \tag{5}$$

where the optical depth $\tau_{a,b}$ is given by

$$\tau_{a,b} \equiv \int_a^b (\alpha_s+\alpha_a)\, dZ \tag{6}$$

The argument θ indicates that the path of integration makes an angle θ with nadir, and the subscript o indicates a surface value. The apparent surface brightness temperature, $T_{BO}(\theta)$ consists of two terms: The radiation emitted by and reflected by the surface.

$$T_{BO} = \varepsilon(\theta)T_o + T_{BR} \tag{7}$$

where ε is the surface emittance, T_o is the surface temperature, and T_{BR} is the reflected sky brightness temperature. The brightness temperature measured by a satellite, then, can be written

$$T_B(\theta) = \left[\varepsilon(\theta)T_o + T_{BR}\right] t_{O,H}(\theta) + \int_0^H t_{Z,H}(\theta)(\alpha_a T + \alpha_s S_c)dZ \tag{8}$$

Qualitatively, equation (8) gives the brightness temperature measured by the satellite as the sum of 1) that portion of the apparent surface brightness temperature which is transmitted through the atmosphere and

2) the brightness temperature which is emitted and scattered into the beam along the atmospheric path and then transmitted to the satellite.

2.2 Transfer Through the Cloudy Atmosphere

The three atmospheric constituents which significantly effect the transfer of microwave radiation are 1) oxygen (O_2), 2) water vapor, and 3) liquid water (Westwater, 1972). Figure 1 shows the approximate atmospheric attenuation due to oxygen and water vapor near the earth's surface and at 4 km.* The peaks near 22, 183, and 323 GHz are water vapor rotation lines (Van Vleck, 1947), while the band near 60 GHz and the line at 118 GHz have been described as oxygen (O_2) "spin reorientation" transitions (Herzberg, 1950). Calculations by Westwater (1972) indicate that the clear atmosphere is more than 60% transparent for frequencies less than 50 GHz (Figure 2). At the Nimbus 5 ESMR frequency of 19.35 GHz (1.55 cm) the clear atmosphere is more than 90% transparent even in the moist tropics.

Deirmendjian (1963) has shown that atmospheric liquid water can be divided into two classes: cloud-size drops and precipitation-size drops. In clouds with modal drop radius less than 50 μm (which includes the vast majority of clouds (Fletcher, 1963)) the scattering of microwave radiation with frequencies less than 60 GHz may be neglected in comparison with absorption. Clouds, therefore, may be treated with a simple absorption coefficient, which is proportional to liquid water content (Westwater, 1972). Figure 3 shows the cloud volume absorption coefficient for a $0^{o}C$ cloud normalized to 1 g m^{-3}. A lower bound on

---

* Attenuation (A) in db km^{-1} is related to volume absorption coefficient (α_a) in km^{-1} by $\alpha_a = (.1 \log_e 10) A \approx 0.2303A$.

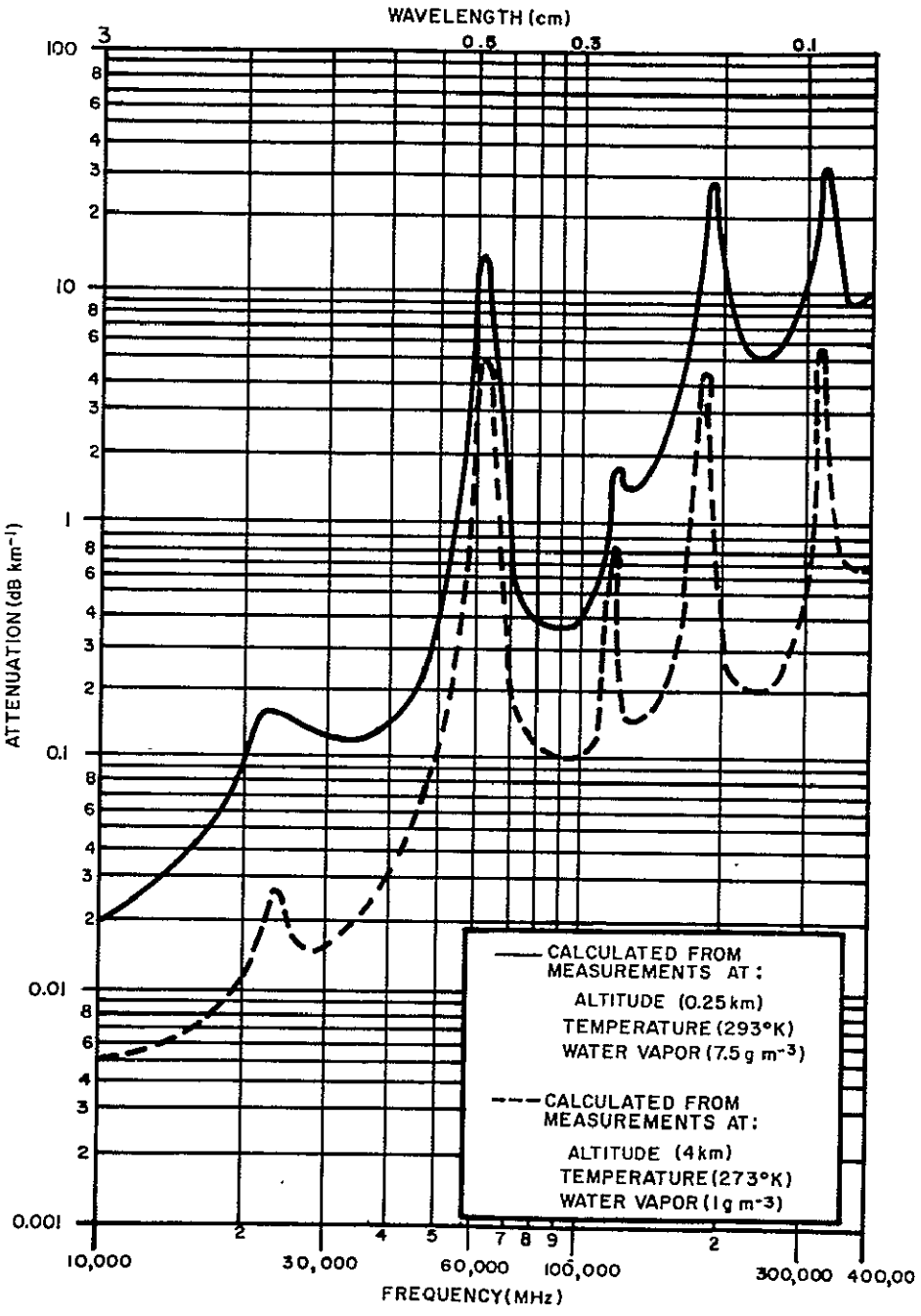

Figure 1. Atmospheric attenuation by combined water vapor and oxygen (O_2). (After Tolbert et al., 1958)

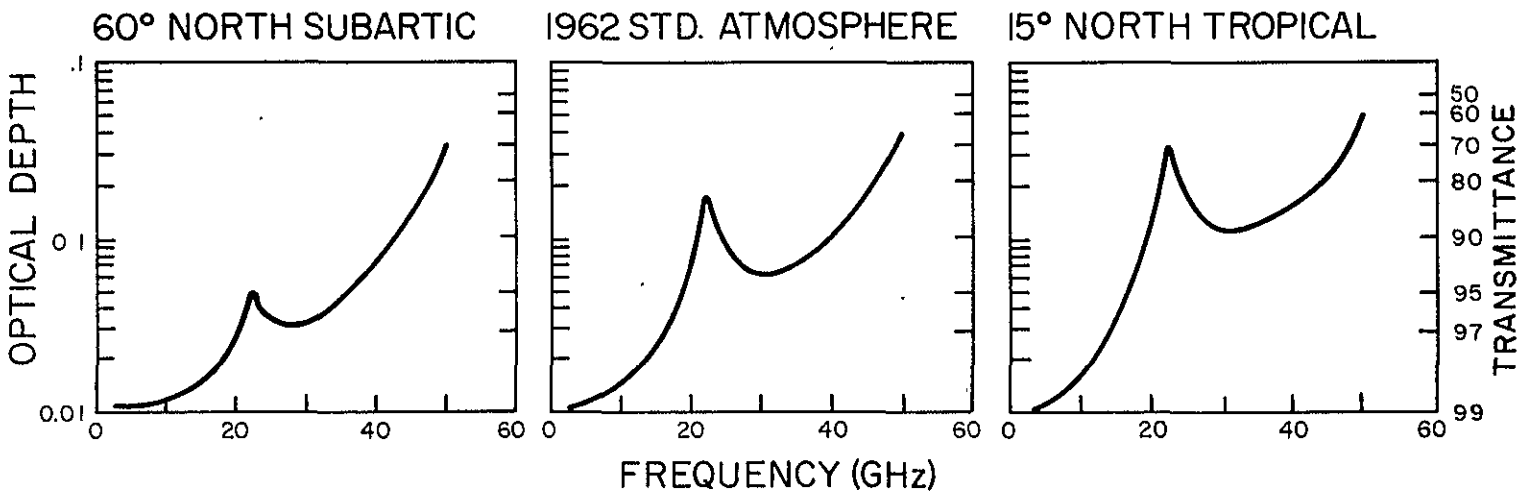

Figure 2. Optical depth of clear atmospheres. (After Westwater, 1972)

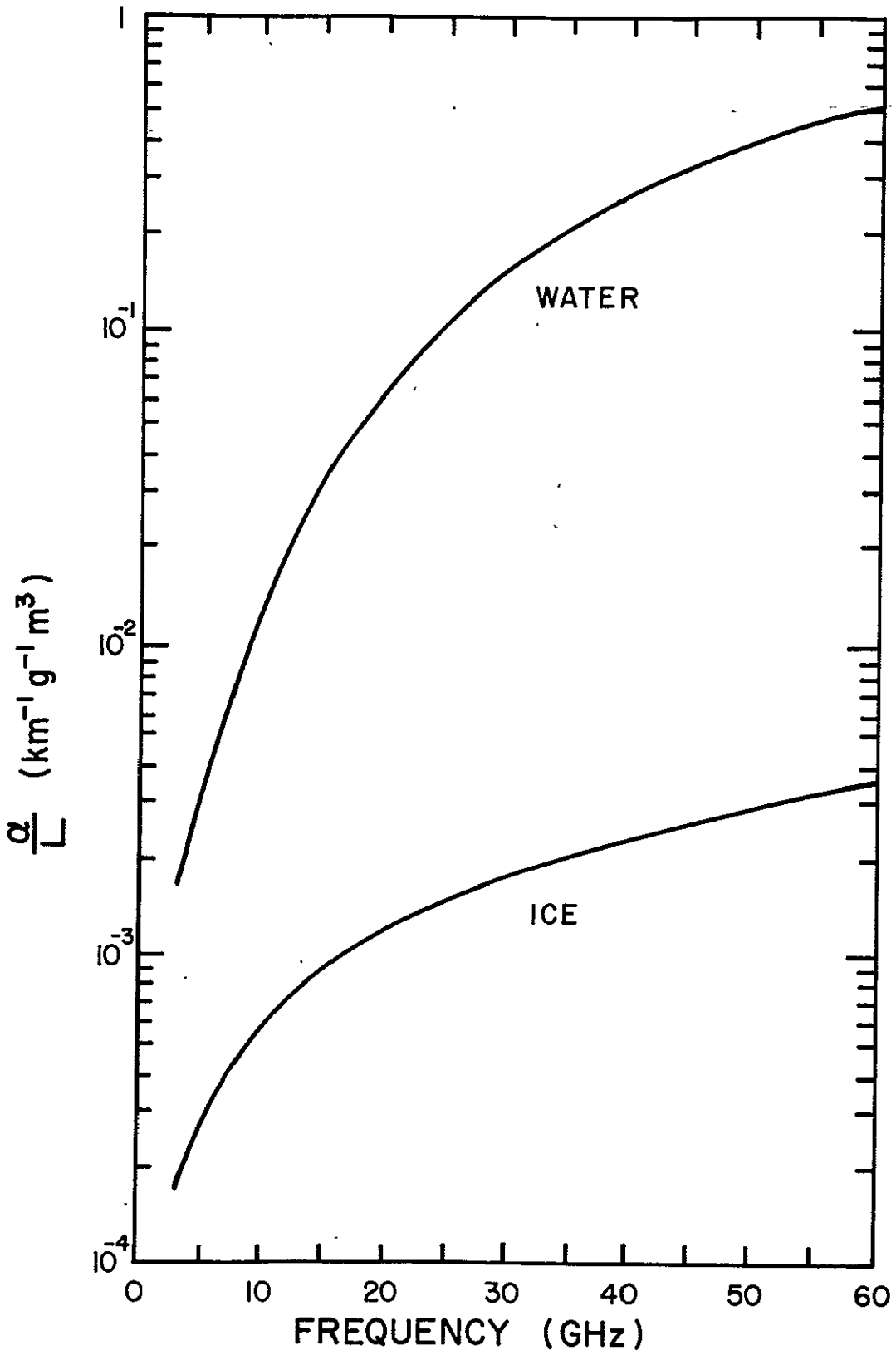

Figure 3. Cloud Optical Depth. (After Westwater, 1972)

cloud transmittance (for nadir viewing) can be obtained as follows

$$\tau_c = \int_0^H \alpha_c \, dZ = \int_0^H \frac{\alpha_c}{L} L \, dZ \qquad (9)$$

where L is the density of the cloud droplets. For frequencies less than 50 GHz, the ratio α_c/L is less than 5 $g^{-1}cm^2$, and for 19.35 GHz, α_c/L is less than 0.8 $g^{-1}cm^2$ for a water cloud.* Ignoring the small temperature dependence of α_c/L,

$$\tau_c \approx \frac{\alpha_c}{L} \int_0^H L dZ = \frac{\alpha_c}{L} L_I \qquad (10)$$

where L_I is the integrated liquid water content of the cloud. Wilheit (1972) estimates a typical value of L_I for a non-raining cloud to be 0.02 g cm^{-2}. Table 1 summarizes the microwave optical properties of non-raining clouds. The total transmittance of the non-raining atmosphere is the product of the clear atmosphere transmittance and the cloud transmittance. At 50 GHz the transmittance is greater than 46%, and at 19.35 GHz it is greater than 85%. This large transmittance through clouds is the chief advantage of passive microwave radiometry.

2.3 Surface Emission

Because the atmosphere is so transparent to microwave radiation of frequencies less than 50 GHz, the surface term in equation (8) is often dominant; the satellite-measured microwave brightness temperature depends strongly on surface emittance.

---

* Ice clouds are much more transparent than water clouds; c,f. Figure 3.

TABLE 1

Approximate Microwave Transmission
Through Non-Raining Clouds

	Typical Cloud	"Thick" Cloud
Integrated Liquid Water	0.02 g cm^{-2}	0.05 g cm^{-2}
Optical Depth		
50 GHz	0.10	0.25
19.35 GHz	0.02	0.04
Transmittance		
50 GHz	90%	77%
19.35 GHz	98%	96%

The emittance of land is a function of soil type and moisture content, but is generally near 0.9. The emittance of ice and snow is a function of its age, but is also near 0.9 (Wilheit, 1972). Continental and polar regions, therefore, appear bright at frequencies less than 50 GHz. The calm ocean, however, has an emittance of less than 0.5 at these frequencies (Wilheit, 1972 and 1975), which causes it to appear cool in comparison to land or sea ice. The 19.35 GHz calm ocean emittance is approximately 0.4. At wind speeds greater than 7 m s^{-1} foam begins to form on the ocean surface, and the emittance increases. For a 25 m s^{-1} wind Nordberg et al. (1971) found a brightness temperature increase of approximately 22 K (at 19.35 GHz) which corresponds to an emittance increase on the order of 0.1 (25%). The effect of wind-induced brightness temperature increases on precipitation frequency estimates will be discussed in Chapter 4.

Calculations* show that the brightness temperature of a plane water surface varies only slightly with temperature (Figure 4) and thus may be regarded as a constant (approximately 120 K at 19.35 GHz). As a function of incident angle, the emittance of a plane water surface decreases for horizontally polarized radiation (Figure 5) but the decrease is only about 10% for angles out to 35^{o} from nadir. This decrease in emittance is partially compensated by the increase of atmospheric emission caused by the increased path length.

A further consequence of the low ocean emittance is that atmospheric constituents are seen in emission, i.e. increasing the amount of water vapor, oxygen, or the density of water droplets in an atmospheric

---

* See Appendix 1.

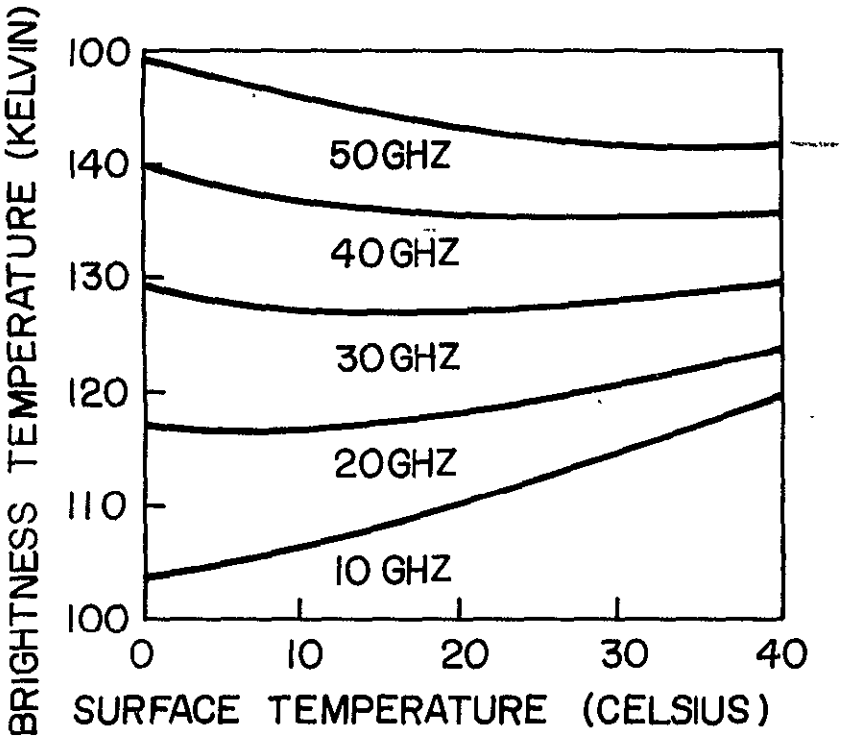

Figure 4. Nadir brightness temperature of a plane water surface versus surface temperature.

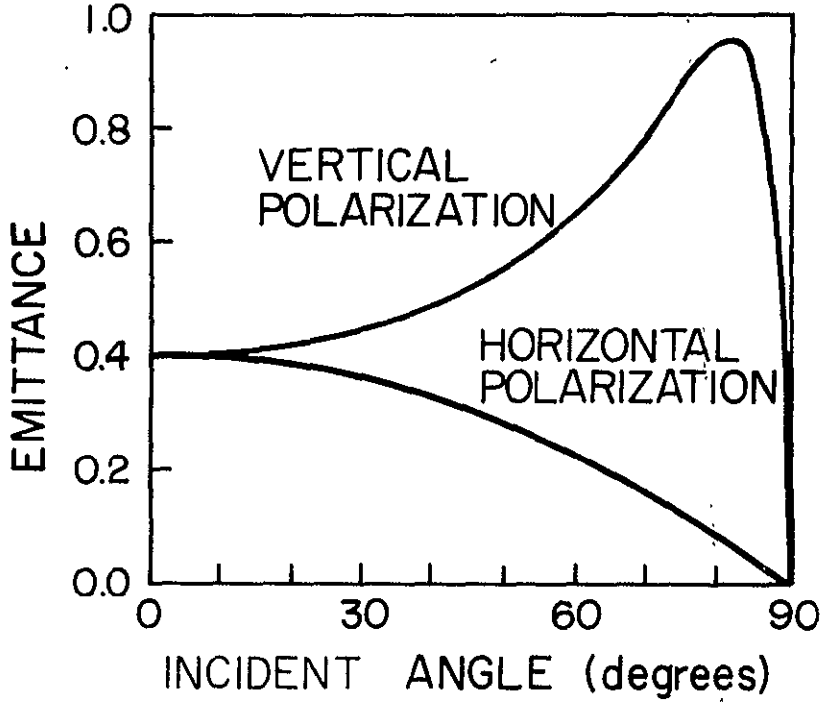

Figure 5. Emittance of a plane water surface versus angle of incidence for a wavelength of 1.55 cm and a surface temperature of 300 K.

column over the ocean generally increases its brightness temperature.* The physical explanation of this phenomenon is that the apparent coolness of the ocean in the microwave spectrum causes an overlying atmospheric parcel to be thermodynamically warmer than its radiative environment; thus it adds to the upwelling radiation stream in the normal process of absorption and reemission.

The fact that atmospheric constituents are seen in emission at microwave frequencies over the ocean leads scientists to believe that passive radiometry might be used to detect these constituents (Shifrin et al., 1968; Staelin, 1969). Among the possibilities are rainfall frequency (the subject of this study), rainfall rate, cloud liquid water, integrated water vapor, and atmospheric temperature.

2.4 Precipitation

Water droplets which are large enough to have significant fall velocities are large enough to interact strongly with microwave radiation. Scattering, therefore, cannot be neglected in rain layers, and one must treat the transfer of microwave radiation through these layers with the full Mie equations (Diermendjian, 1963). Wilheit et al.(1975) have used a Marshall-Palmer dropsize distribution and Mie scattering theory to calculate the 19.35 GHz brightness temperature as a function of rainfall rate and freezing level over the ocean. Their preliminary results (Figure 6) compare favorable with radar-measured and rain gauge-measured rainfall rates.

---

* Except at very high rainfall rates. See Figure 6.

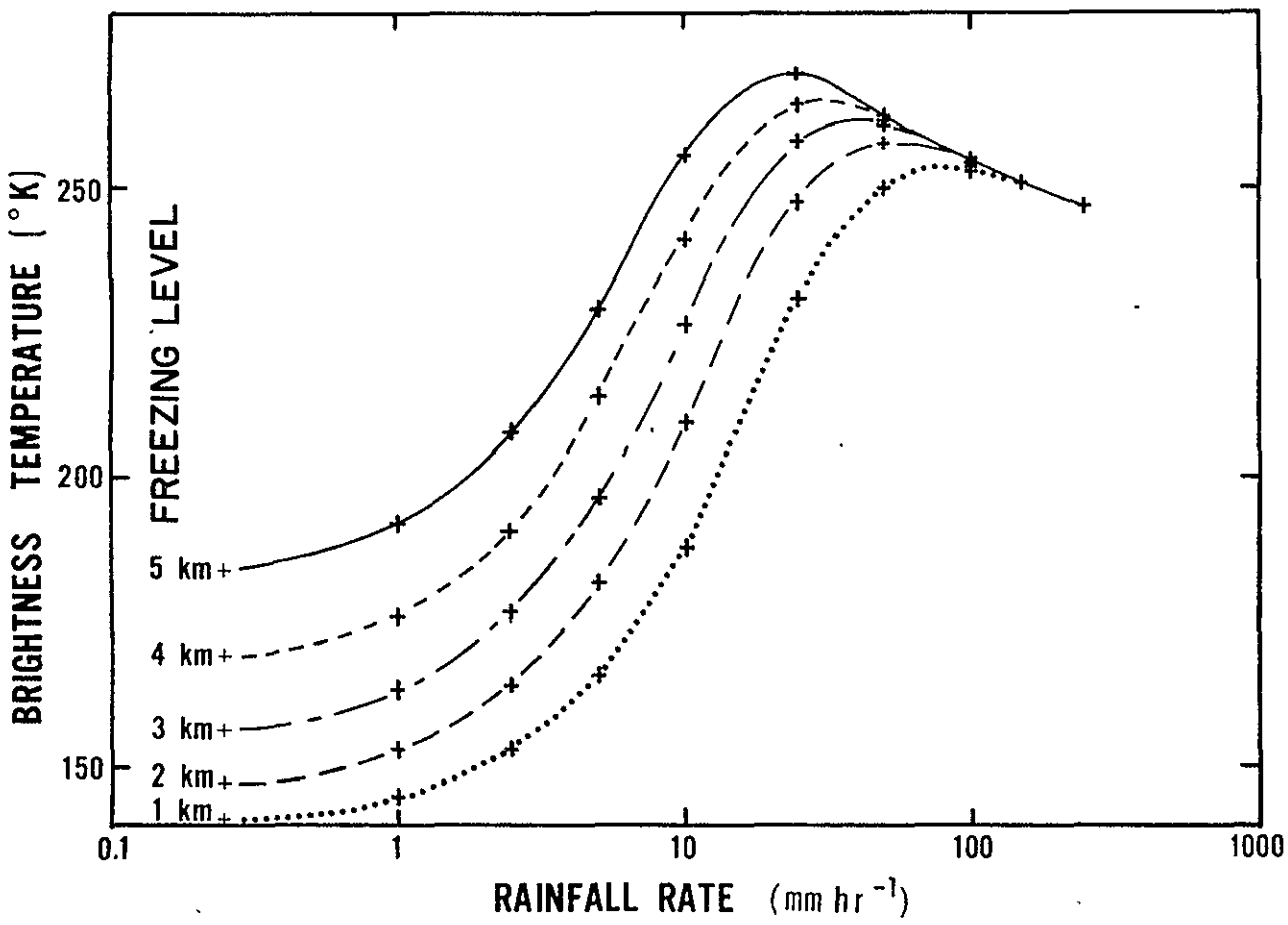

Figure 6. 1.55 cm brightness temperature versus rainfall rate. (After Wilheit et al., 1975

It should be noted that because the complex part of the index of refraction of ice is much less than that of water, ice clouds are much poorer absorbers of microwave radiation than are water clouds. Thus ice clouds may be neglected when calculating the transfer of microwave radiation (Battan, 1973). Similarly dry snow does not interact well with microwave radiation. While a rain layer is rather opaque at centimeter wavelengths, a dry snow layer is virtually transparent (Battan, 1973). Thus the freezing level may be used to indicate the thickness of the rain layer, and the frozen precipitation above the layer may be ignored in the scattering calculations.

The results of Wilheit et al. form the basis of a thresholding technique used in this paper for the detection of oceanic precipitation described in Section 3.4.

3.0 DATA AND ANALYSIS

3.1 Description of the Radiometer

The Electrically Scanning Microwave Radiometer (ESMR) carried aboard Nimbus 5 was launched 11 December 1972 into a sun-synchronous orbit and became operational 19 December 1972. The radiometer consists of three major components.*

1. A nadir-pointing, phased array antenna (Figure 7) consisting of 103 wave guides in a 83.3 cm by 85.5 cm rectangle which detects horizontally polarized radiation ($\vec{E}$ parallel to the spacecraft velocity vector.)

2. A beam-steering computer which sweeps the received beam from 50^{o} left to 50^{o} right of the spacecraft track in 78 steps every four seconds by means of an electronic phase shifter in each wave guide.

3. A microwave receiver operating with a center frequency of 19.35 GHz and a bandwidth of 250 MHz. A 10 MHz band centered on 19.35 GHz is not received.

The ground resolution is 25 km by 25 km at nadir, approximately 42 km crosstrack by 30 km downtrack at 30^{o} from nadir, and degrades to 160 km crosstrack by 45 km downtrack at 50^{o} from nadir (Figure 8). Thus an ESMR scan spot covers approximately 500 km^2 at nadir and 1000 km^2 at 30^{o} from nadir.

The Nimbus 5 orbit (81^{o} retrograde inclination, approximately 1100 km altitude) is such that ESMR views every point on earth at least twice per day (if one uses all of the data from $\pm 50^{o}$ from nadir). It crosses the equator at 1130** (ascending) and 2330*** (decending)

---

* See Wilheit (1972) for a more complete description.

** "Noon"

*** "Midnight"

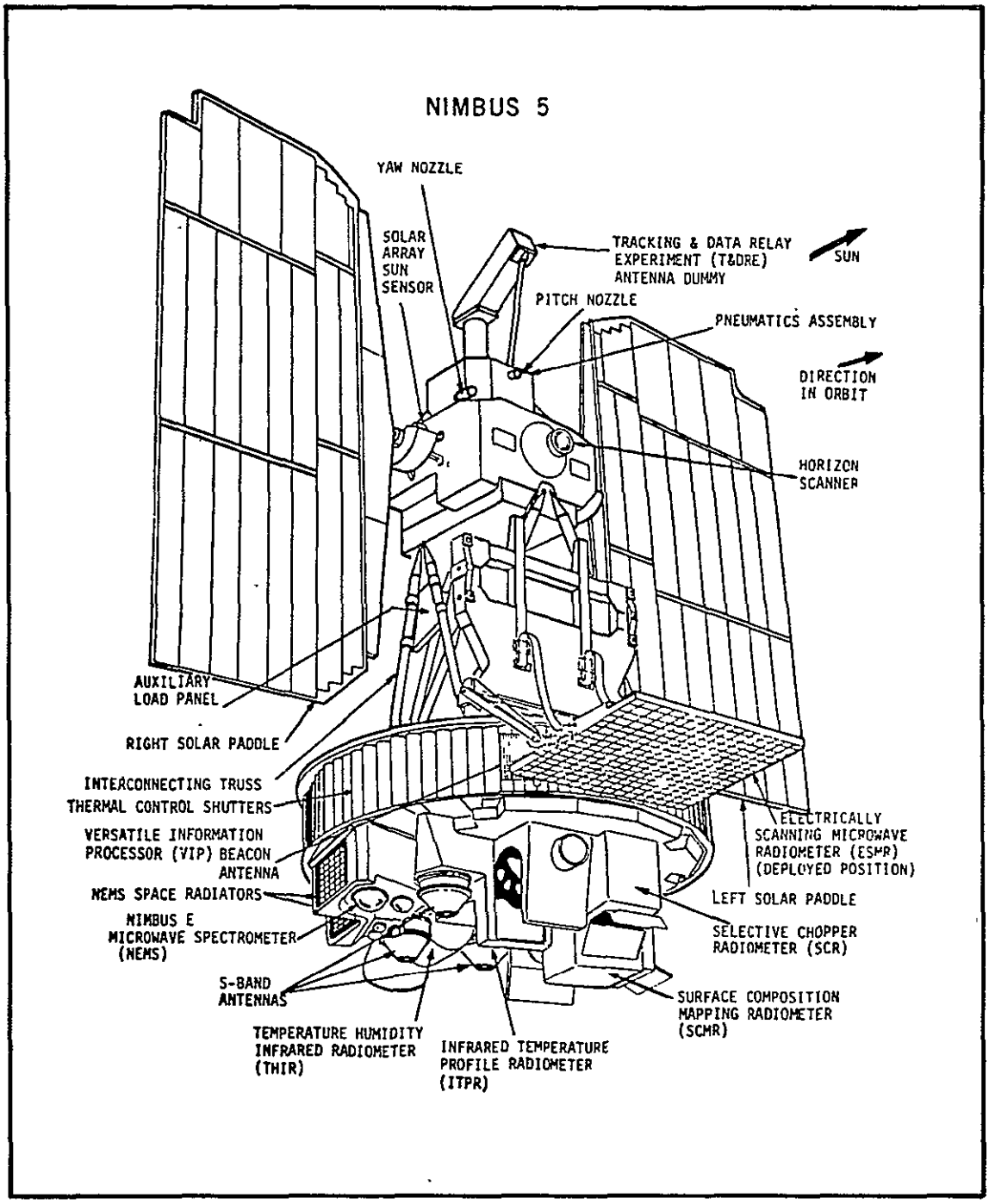

Figure 7. The Nimbus 5 spacecraft. (from The Nimbus 5 User's Guide.)

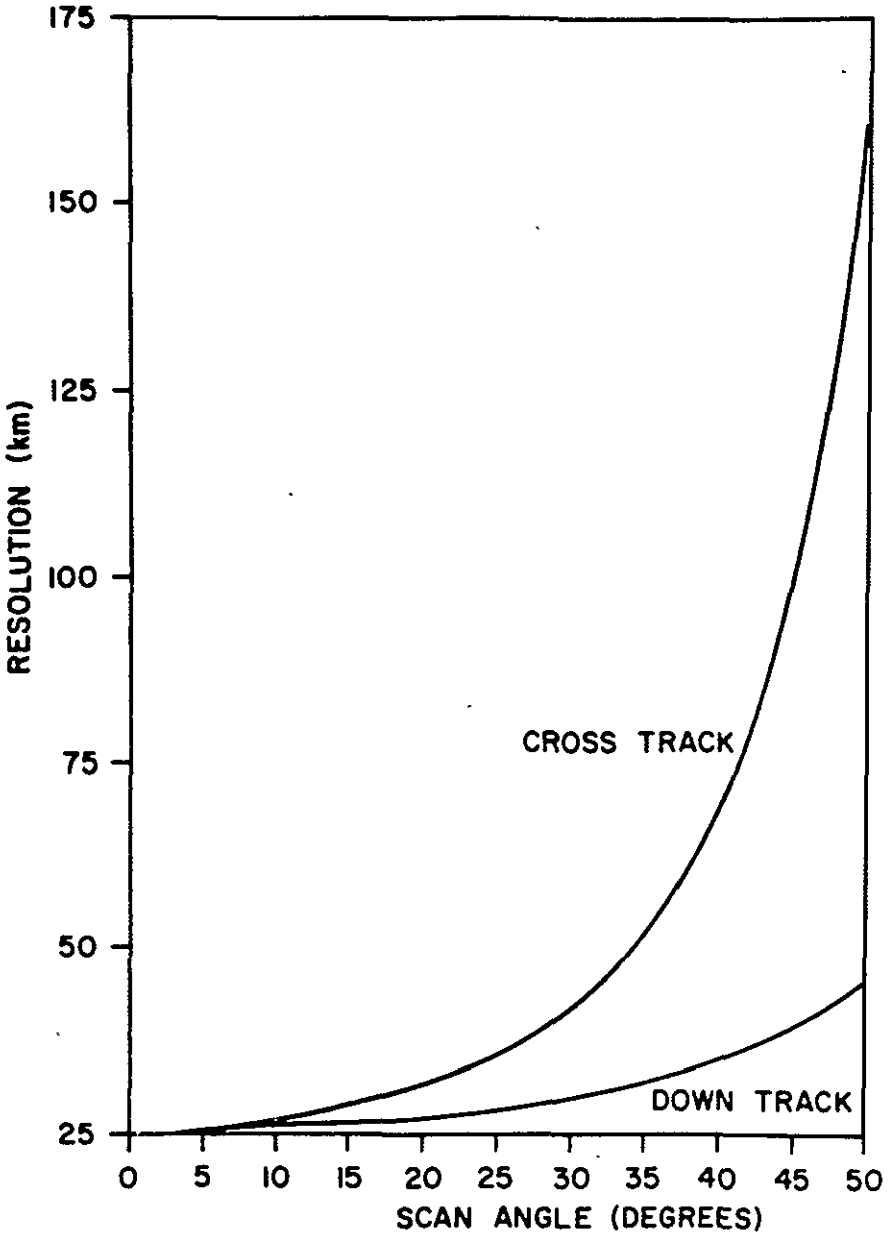

Figure 8. Resolution of the Electrically Scanning Microwave Radiometer. (After Wilheit, 1972)

local time and has an orbital period of approximately 107 minutes. Additional ESMR characteristics are noted in Appendix 2.

Figure 9 is a montage of photographically processed ESMR data from The Nimbus 5 Data Catalog, Vol. 1 in which brightness temperatures greater than 250 K appear black, those less than 190 K appear white, and those in between are represented with a linear gray scale. The darkest regions over the ocean are areas of intense rain, while the gray areas represent lighter rainfall rates (See Figure 6). Cloudy but non-raining areas have brighness temperatures less than 190 K and thus cannot be seen in this picture.

3.2 The Data Set

The Nimbus 5 ESMR data used in this study were recorded during the period 22 December 1972 through 26 February 1973. Approximately one half of the available data were randomly selected for study to reduce the bulk processing. Figure 10 shows the distribution of the selected data in number of orbits per day -- 13 1/3 being the maximum daily number. The data are recorded on Calibrated Brightness Temperature (CBT) Tapes* which contain the position (latitude, longitude) of each scan spot, time, subsatellite point, and various calibration data in addition to the brightness temperatures.

---

* These tapes are available from The National Space Science Data Center, Greenbelt, MD, and are described in detail in The Nimbus 5 User's Guide and The Nimbus 5 Data Catalog.

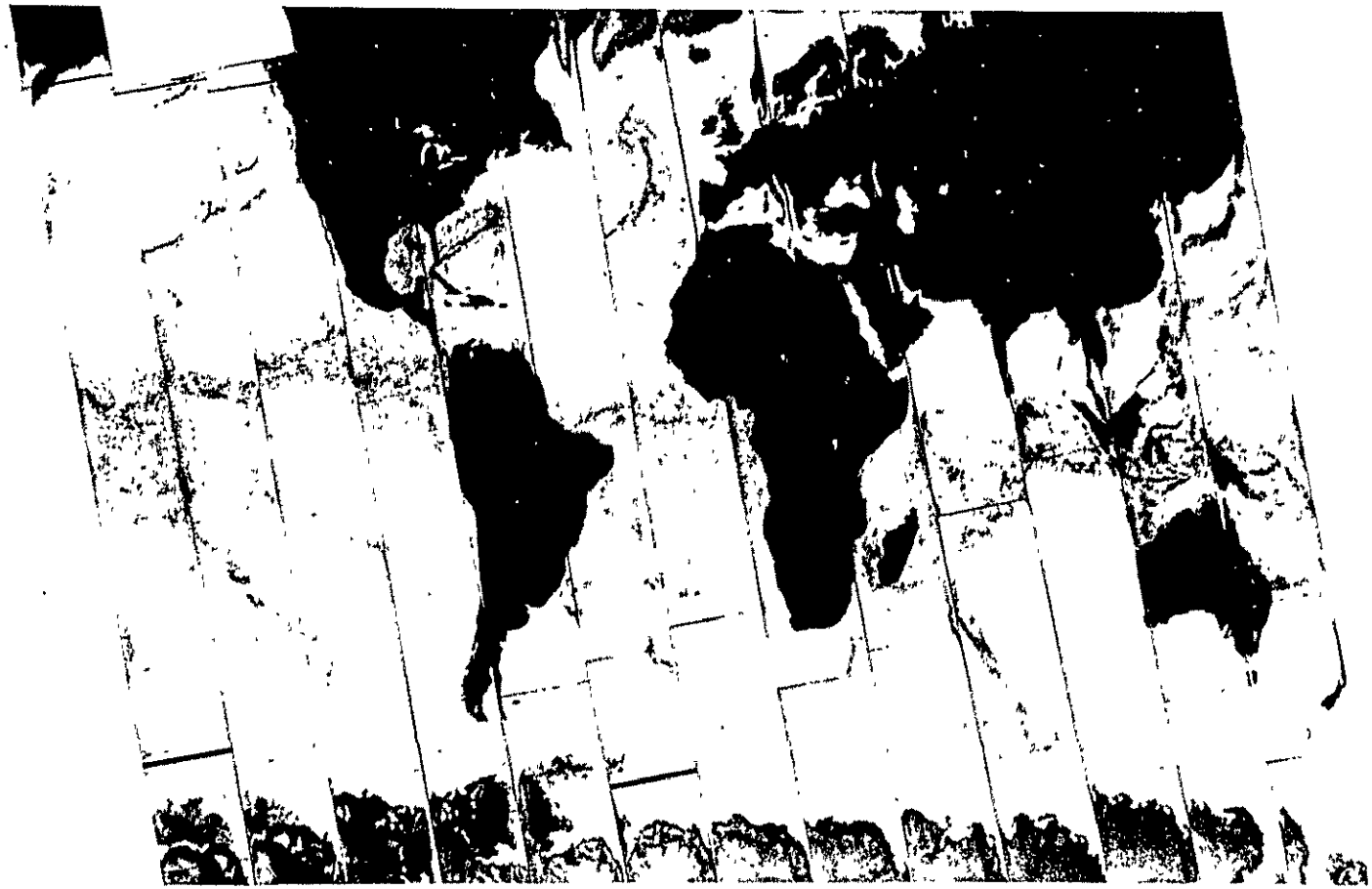

Figure 9. Photographically processed Nimbus 5 ESMR data from 11 January 1973, orbits 413-425. Brightness temperatures less than 190 K are white, those greater than 250 K are black, and those in between are represented by a linear gray scale. Rain, which appears dark over the ocean is evident in the tropics and in several weather fronts. (From The Nimbus 5 Data Catalog, Vol. 1)

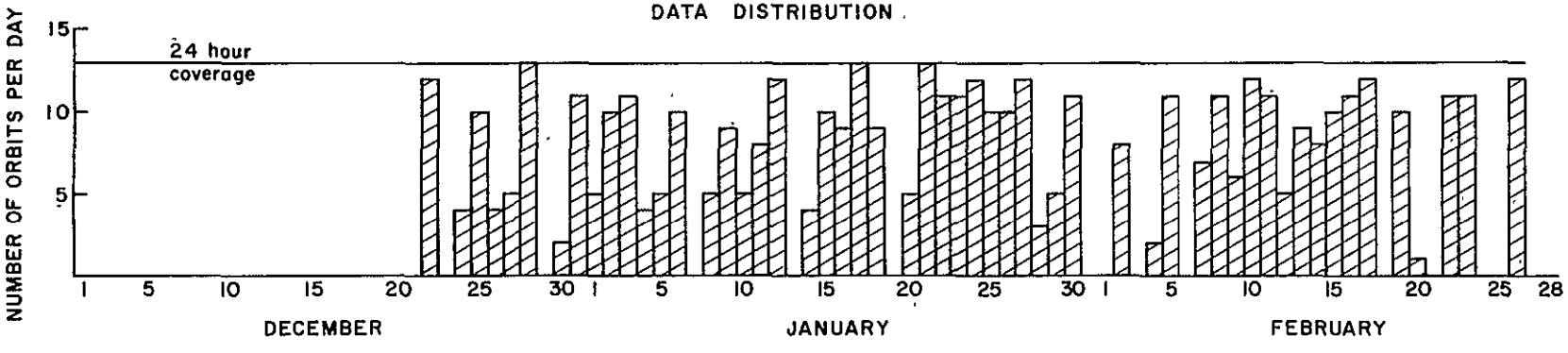

Figure 10. Distribution of the Nimbus 5 ESMR data used in this study

3.3 Angular Corrections

To eliminate a cross-polarization lobe problem with the ESMR antenna, the brightness temperatures on the CBT Tapes have been corrected by the National Aeronautics and Space Administration (NASA) with a linear empirical correction first described in Volume 2 of The Nimbus 5 Data Catalog. NASA's correction was applied to all of the data regardless of surface type or local time while the CBT Tapes were being made. No correction was found necessary near nadir.

In the course of this study it was determined that the correction applied by NASA does not fully eliminate the problem of brightness temperature variation with scan angle over the ocean. We also found that there is a small offset between midnight and noon data. To examine and hopefully resolve these problems, the Pacific Ocean data were partitioned into 10^{o} latitude-longitude squares and the mean brightness temperature for the three months was calculated as a function of the scan angle for each square. Then the difference between the mean brightness temperature at scan angle θ and the mean brightness temperature at nadir (actually the two beam positions at $\pm$ 0.6^{o} from nadir) was averaged over all 104 10^{o} latitude-longitude squares and plotted versus θ. The results for the local noon data are shown in Figure 11a. When the local midnight data were analyzed, they were found to be cooler than the local noon data. In 15 squares which receive little rain, the average difference between the noon and midnight brightness temperatures was found to be 5.8 K $\pm$ 0.9 K. Figure 11b shows the mean midnight T_B versus θ data, but the curve has been shifted down 5.8 K to correct for the apparent day-night temperature difference which is not physically reasonable. The two curves in Figure 11 constitute

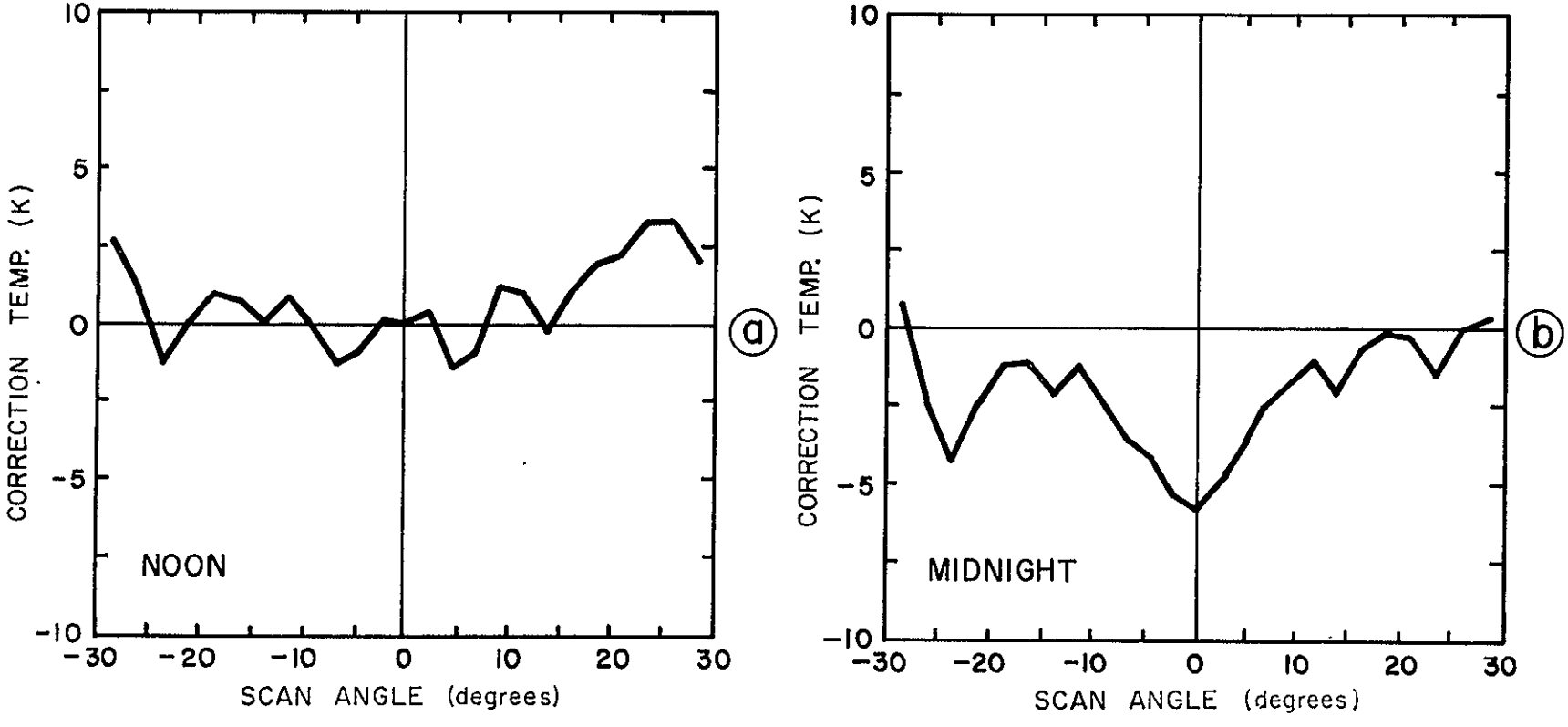

Figure 11. Scan angle correction temperatures, (a) noon correction, (b) midnight correction.

correction curves which will make the three-month mean brightness temperatures independent of scan angle and local time. Table 2 lists the exact correction temperatures used.* These temperatures were subtracted from the temperatures in the CBT Tapes before application of the thresholding technique described below.

3.4 The Use of a Threshold Brightness Temperature to Detect Oceanic Precipitation

Radiative transfer theory predicts that at 1.55 cm a rain layer should appear bright against the cold background of the ocean. The photographically processed Nimbus 5 ESMR data corroborates this theory. The purpose of this study was to determine a threshold brightness temperature which can be used to detect oceanic precipitation and to use this temperature to calculate seasonal mean precipitation frequencies for the oceans.

Because the seasonal mean freezing level is zonal in character (Figure 12), zonal mean freezing levels (Figure 13, Table 3) were combined with the brightness temperature-rainfall rate curves of Wilheit et al. (1975) (Figure 6) to yield zonal threshold temperatures for the detection of five rainfall rates (Figure 14, Table 4).

The algorithm for calculating precipitation frequencies is the following. For each oceanic 5^{o} latitude-longitude square between 30^{o}N and 30^{o}S the brightness temperature data from the CBT Tapes are first corrected for scan angle with the correction listed in Table 2 and then

---

* In the above-mentioned analysis program, data for two adjacent beam positions were combined. Thus the correction is actually an average for the two beam positions and the same correction is applied to each beam position.

TABLE 2

Scan Angle Correction Temperatures
(To be subtracted from CBT Tape data)

Beam Positions	Nominal Scan Angles	Temperature Correction (K) Noon	Midnight
	(degrees)		
15-16	-29.2 & -27.9	2.7	0.8
17-18	-26.6 & -25.3	1.0	-2.5
19-20	-24.1 & -22.8	-1.2	-4.4
21-22	-21.6 & -20.4	0.1	-2.5
23-24	-19.2 & -18.0	1.0	-1.2
25-26	-16.8 & -15.6	0.8	-1.1
27-28	-14.4 & -13.2	0.0	-2.1
29-30	-12.1 & -10.9	0.8	-1.2
31-32	-9.7 & -8.6	-0.1	-2.4
33-34	-7.4 & -6.3	-1.3	-3.5
35-36	-5.1 & -4.0	-0.9	-4.1
37-38	-2.9 & -1.7	0.1	-5.3
39-40	-0.6 & 0.6	0.0	-5.8
41-42	1.7 & 2.9	0.4	-4.9
43-44	4.0 & 5.1	-1.4	-3.8
45-46	6.3 & 7.4	-0.9	-2.4
47-48	8.6 & 9.7	1.2	-1.7
49-50	10.9 & 12.1	1.0	-1.0
51-52	13.2 & 14.4	-0.3	-2.1
53-54	15.6 & 16.8	1.0	-0.6
55-56	18.0 & 19.2	1.9	-0.1
57-58	20.4 & 21.6	2.2	-0.2
59-60	22.8 & 24.1	3.2	-1.4
61-62	25.3 & 26.6	3.3	0.1
63-64	27.9 & 29.2	1.9	0.4

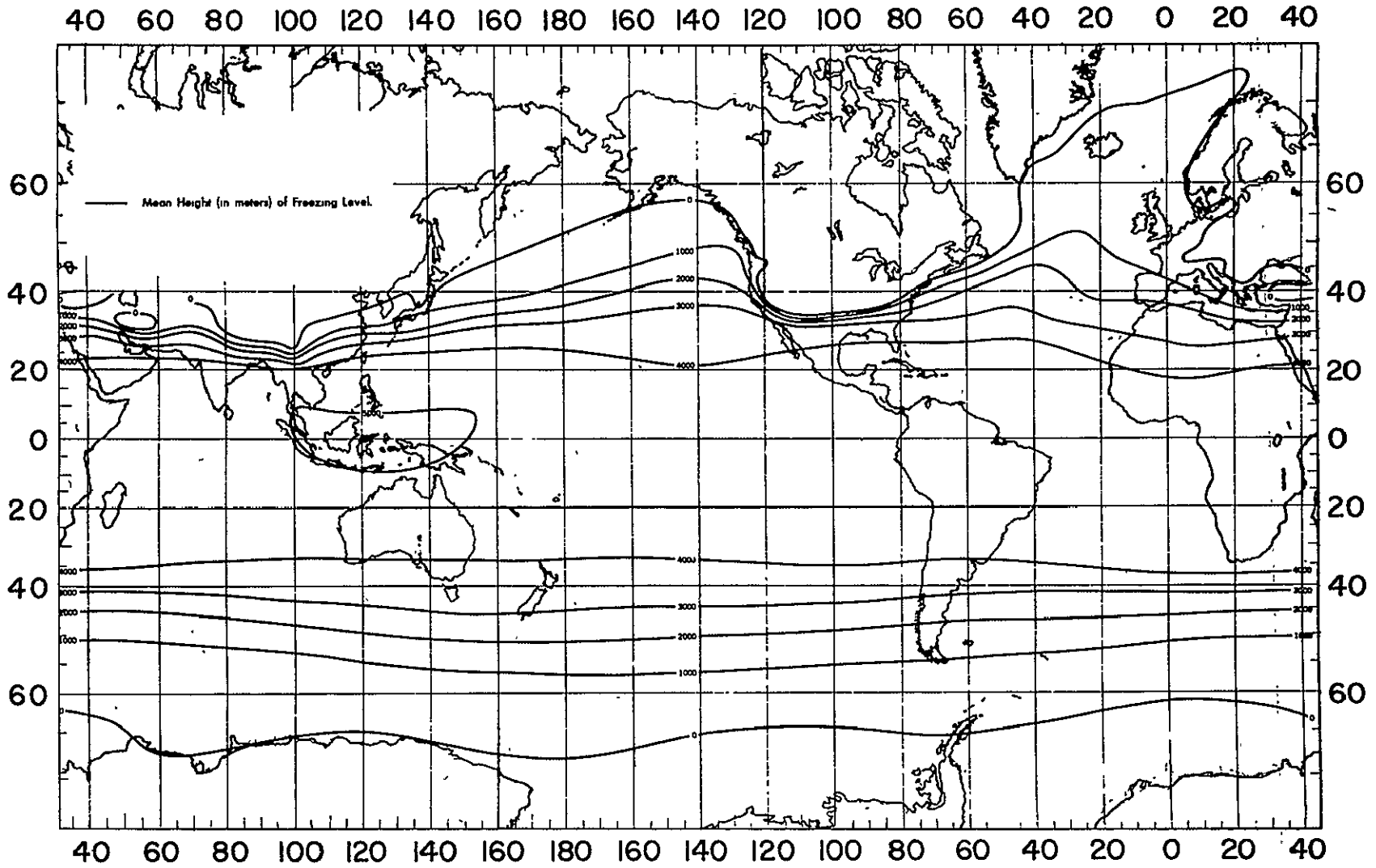

Figure 12. Mean freezing level for the season December-January-February. (After Crutcher and Davis, 1969)

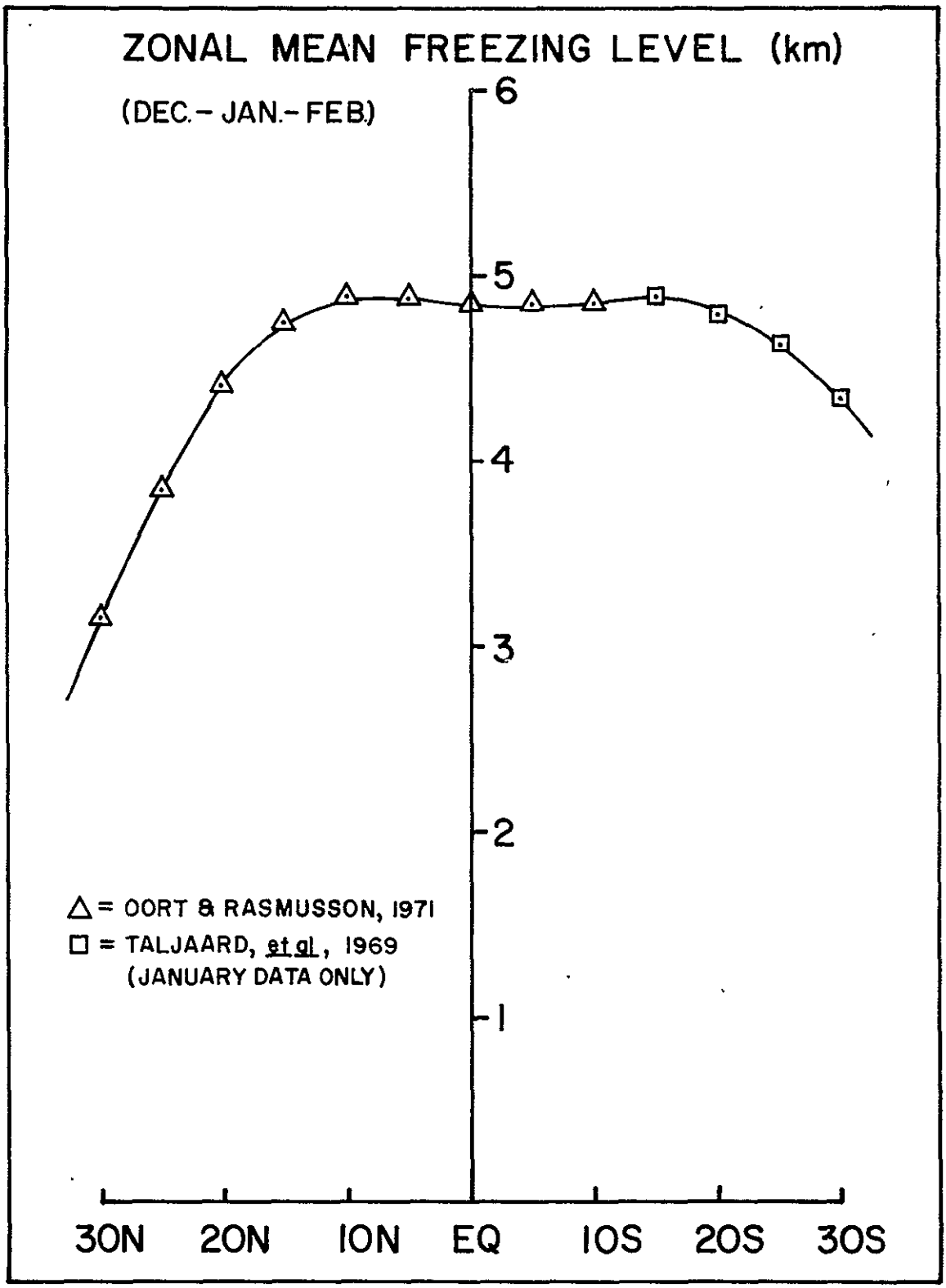

Figure 13. Zonal mean freezing levels for the season December-January-February. (After Oort and Rasmussen, 1971 and Taljaard et al., 1969)

TABLE 3

Zonal Mean Freezing Levels for the Season December-January-February. (After Oort and Rassmussen, 1971; and Taljaard et al., 1969)

Zone	Mean Freezing Level (km)
$30^{o}S$ - $25^{o}S$	4.48
$25^{o}S$ - $20^{o}S$	4.71
$20^{o}S$ - $15^{o}S$	4.84
$15^{o}S$ - $10^{o}S$	4.89
$10^{o}S$ - $5^{o}S$	4.87
$5^{o}S$ - EQ	4.86
EQ - $5^{o}N$	4.86
$5^{o}N$ - $10^{o}N$	4.88
$10^{o}N$ - $15^{o}N$	4.81
$15^{o}N$ - $20^{o}N$	4.58
$20^{o}N$ - $25^{o}N$	4.13
$25^{o}N$ - $30^{o}N$	3.50

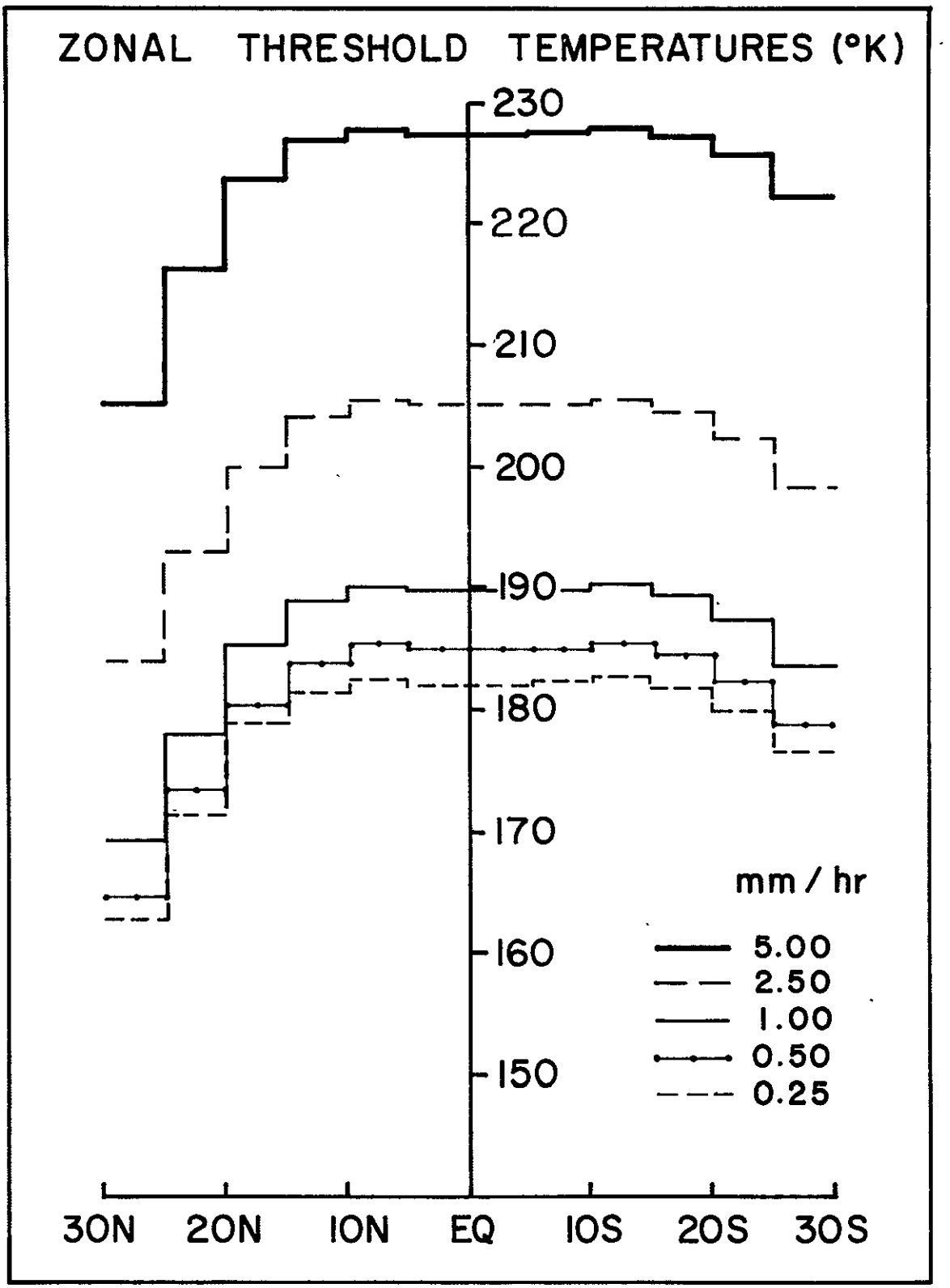

Figure 14. Zonal 1.55 cm threshold brightness temperatures for the detection of oceanic precipitation during the season December-January-February.

TABLE 4

1.55 cm Zonal Threshold Brightness Temperatures
For the Detection of Oceanic Precipitation
During the Season December-January-February

Zone	Threshold Brightness Temperature (K)				
	0.25 mm hr^{-1}	0.5 mm hr^{-1}	1.0 mm hr^{-1}	2.5 mm hr^{-1}	5.0 mm hr^{-1}
$30^{o}S$ - $25^{o}S$	176.6	178.8	183.6	198.4	222.1
$25^{o}S$ - $20^{o}S$	180.0	182.5	187.3	202.3	225.5
$20^{o}S$ - $15^{o}S$	181.9	184.5	189.4	204.7	227.1
$15^{o}S$ - $10^{o}S$	182.6	185.4	190.3	205.7	227.7
$10^{o}S$ - $5^{o}S$	182.4	185.0	189.9	205.3	227.5
$5^{o}S$ - EQ	182.2	184.9	189.8	205.1	227.4
EQ - $5^{o}N$	182.2	184.9	189.8	205.1	227.4
$5^{o}N$ - $10^{o}N$	182.5	185.2	190.1	205.5	227.6
$10^{o}N$ - $15^{o}N$	181.5	184.1	188.9	204.2	226.8
$15^{o}N$ - $20^{o}N$	178.1	180.4	185.2	200.0	223.6
$20^{o}N$ - $25^{o}N$	171.4	173.4	178.2	192.9	216.3
$25^{o}N$ - $30^{o}N$	162.7	164.6	169.4	184.0	205.2

are compared with the threshold temperatures listed in Table 4. Only data with scan angles between $\pm 30^{o}$ from nadir are used. The number of observations which lie above each of the threshold temperatures is recorded along with the total number of observations, midnight and noon observations being kept separate. The results are presented and discussed in the next chapter.

4.0 RESULTS

4.1 Tropical Oceanic Precipitation Frequency

Figure 15 shows the frequency, in percentage of observations, of oceanic precipitation for the season December 1972 through February 1973 based on the assumption that the 0.25 mm hr^{-1} brightness temperatures in Table 4 represent the rain - no rain threshold temperatures. (The noon and midnight frequencies have been averaged.) Several expected characteristics of oceanic precipitation are readily apparent:

1. Narrow convergence zones extending around the earth near the equator.
2. Dry eastern oceans.
3. The splitting of the Intertropical Convergence Zone (ITCZ) in the mid-Pacific and a tendancy for such splitting in the western Atlantic.
4. A mid-Pacific maximum in precipitation frequency (23% in the 5^{o} latitude-longitude square centered at $7.5^{o}S$, $172.5^{o}W$.)

These results may be compared with the data of McDonald (1938) who compiled 50 years of ship log weather observations taken at Greenwich noon. A portion of his Chart 95 is shown in Figure 16. Although McDonald found generally higher frequencies, the overall agreement is good. His maximum frequency is approximately 30% at $7^{o}S$, $163^{o}E$. More recently Taylor (1973) has compiled An Atlas of Pacific Islands Rainfall, which gives an indication of oceanic precipitation frequencies, (see below). Figure 17 shows the mean January precipitation in millimeters. The contours are very similar to those of Figure 15; but, again, the Pacific precipitation maximum during the season December 1972 through February 1973 was approximately 20^{o} east of its normal position.

C.S. Ramage (1975) points out, however, that December 1972 through February 1973 was an anomalous period in the tropical Pacific (if not

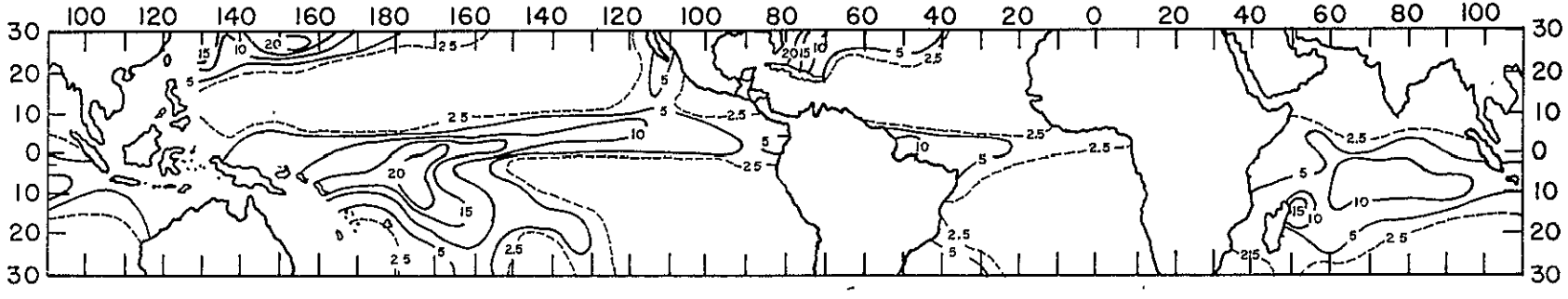

Figure 15. Frequency of precipitation (in percent of observations) for the season December 1972 through February 1973 as derived from Nimbus 5 ESMR data. (The noon and midnight frequencies have been averaged).

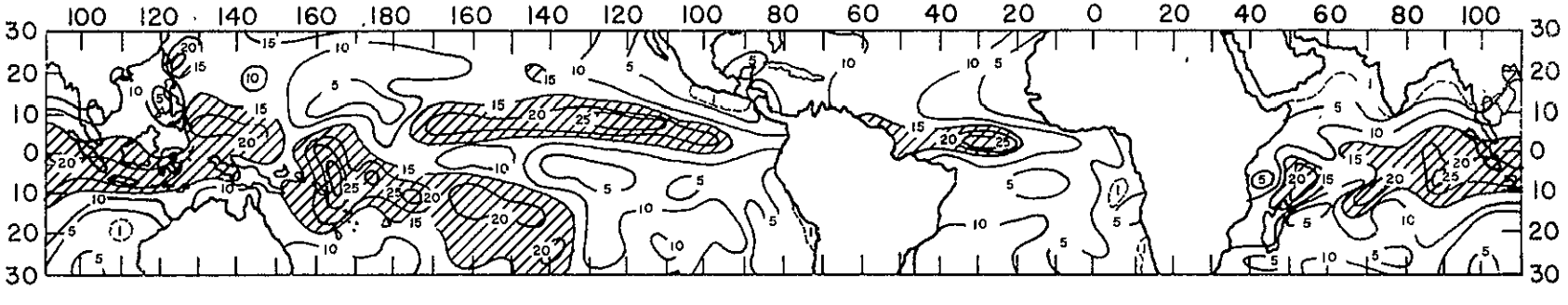

Figure 16. Frequency of precipitation (in percent of observations) for the season December-January-February from ship observations taken at Greenwich noon. (After McDonald, 1938).

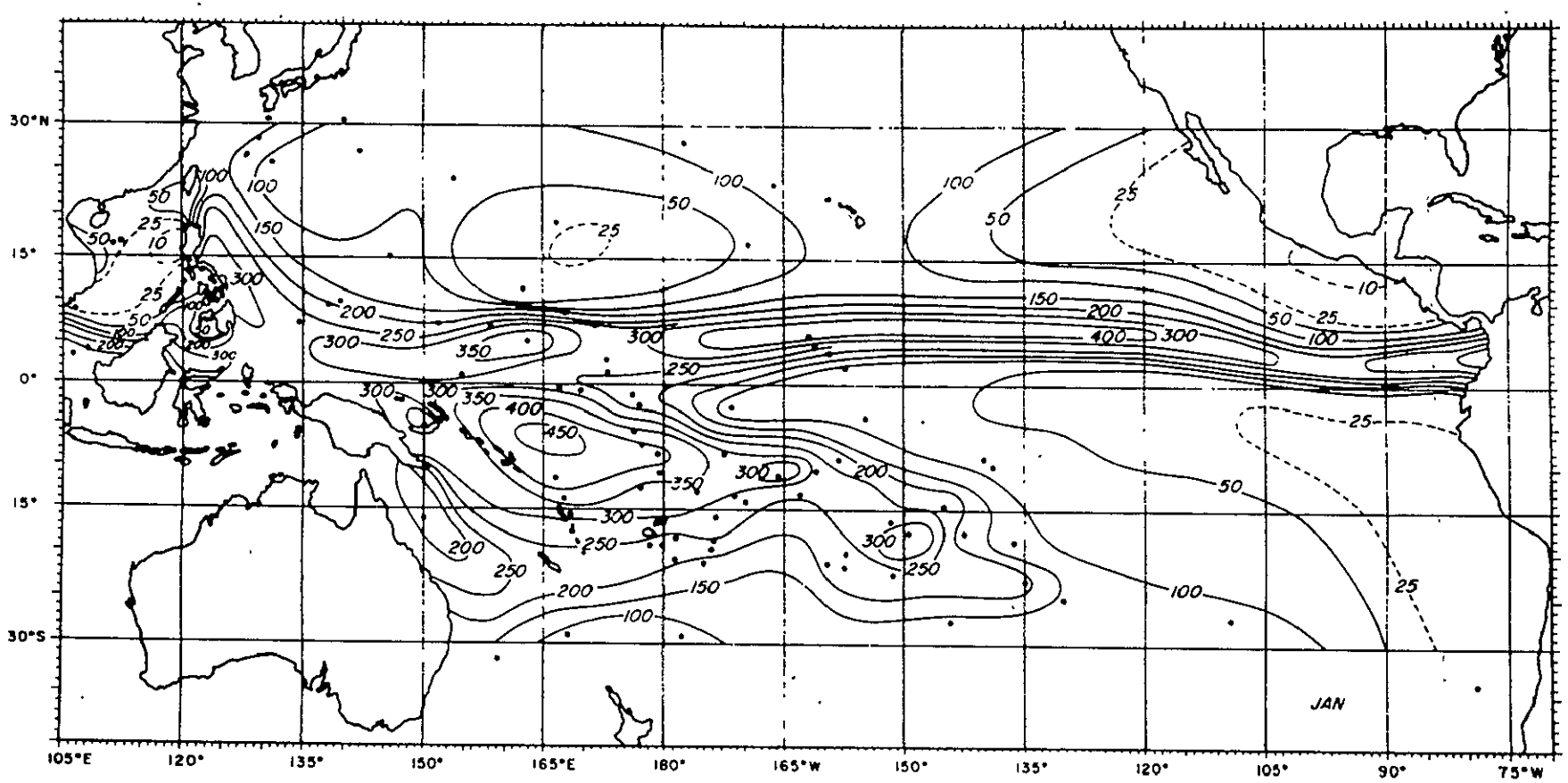

Figure 17. Mean January precipitation (mm). (After Taylor, 1973)

in the entire world). In this study of the 1972-1973 El Niño, Ramage calculated the frequency of highly reflective clouds from National Environmental Satellite Service daily digitized visible cloud pictures (Figures 18 and 19). Although the connection between visible cloud brightness and precipitation is much less clear physically than that between microwave brightness temperature and precipitation, Figures 18 and 19 show that the cloudiness distribution in December 1972 (the contours of which closely resemble the contours of precipitation frequency found in this study) are rather different from the more normal distribution in December 1971.

As mentioned in Chapter 3, wind, by causing foam formation on the sea surface, can increase the microwave brightness temperature and bias precipitation frequency measurements. An estimate of the magnitude of this problem can be obtained from Figure 20 which shows the frequency of Beaufort force 7 (15.5 m s^{-1}) or higher winds at Greenwich noon in January (after McDonald, 1938). Throughout most of the tropical oceans there does not seem to be frequent enough wind to significantly bias the results of this study. However, the northwest oceans seem to have more frequent winds, thus the precipitation frequencies for those areas may be overestimated.

Using the other threshold temperatures in Table 4, one can investigate the frequencies of occurrence of various rainfall intensities. Figures 21 through 23 were constructed by stratifying the data using 0.25 mm hr^{-1} as the threshold for light rain, 1.0 mm hr^{-1} for moderate rain, and 2.5 mm hr^{-1} for heavy rain. (Again, noon and midnight frequencies were averaged.) This stratification places approximately one third of the total rain observations in each category. Generally the

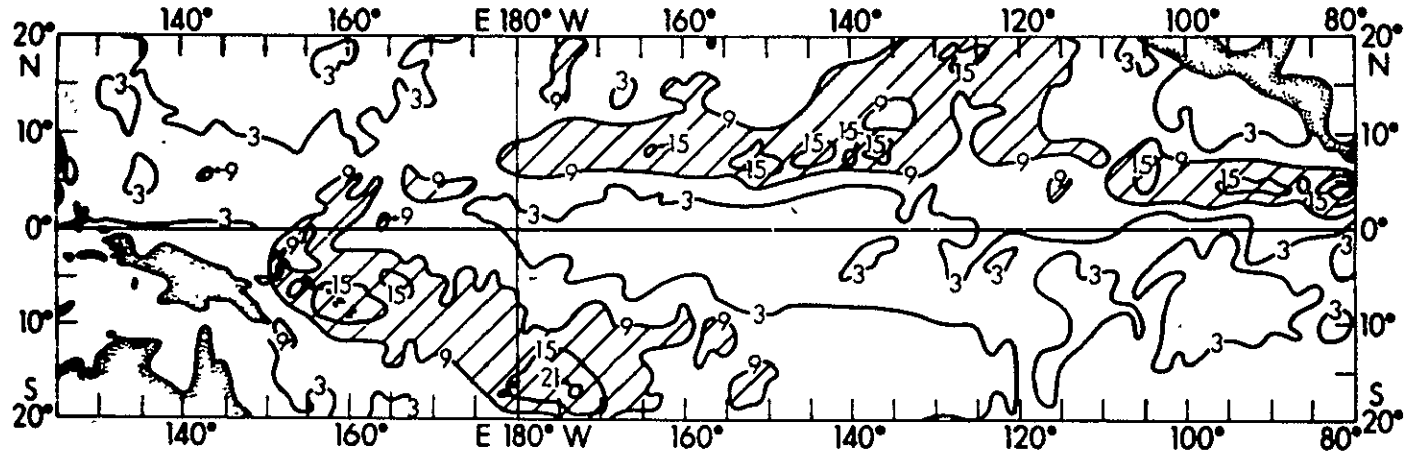

Figure 18. Frequency of highly reflective clouds for December 1971. (After Ramage, 1975)

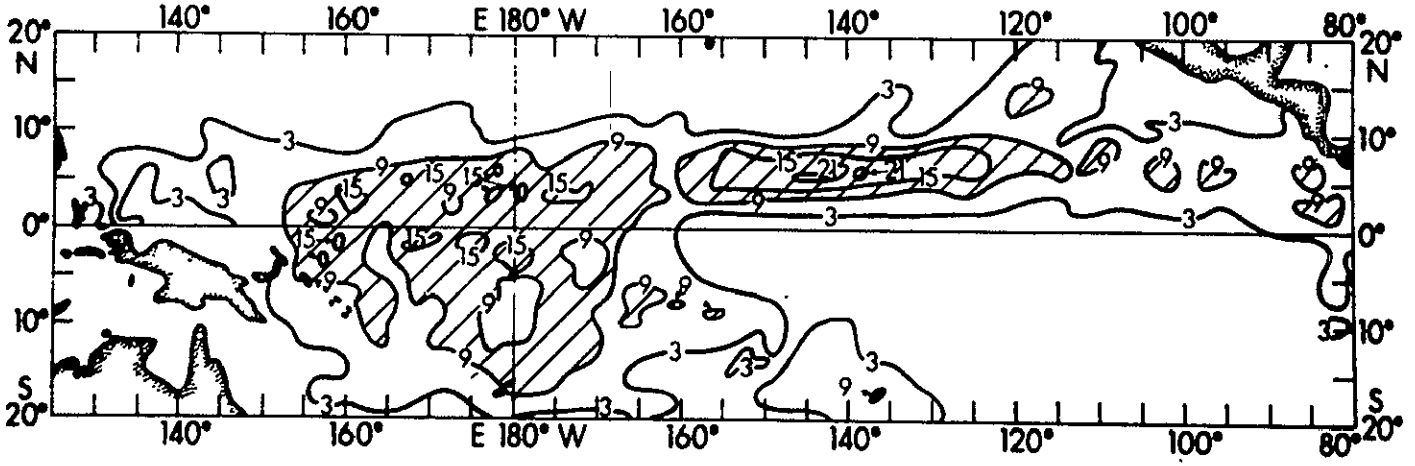

Figure 19. Frequency of highly reflective clouds for December 1972. (After Ramage, 1975)

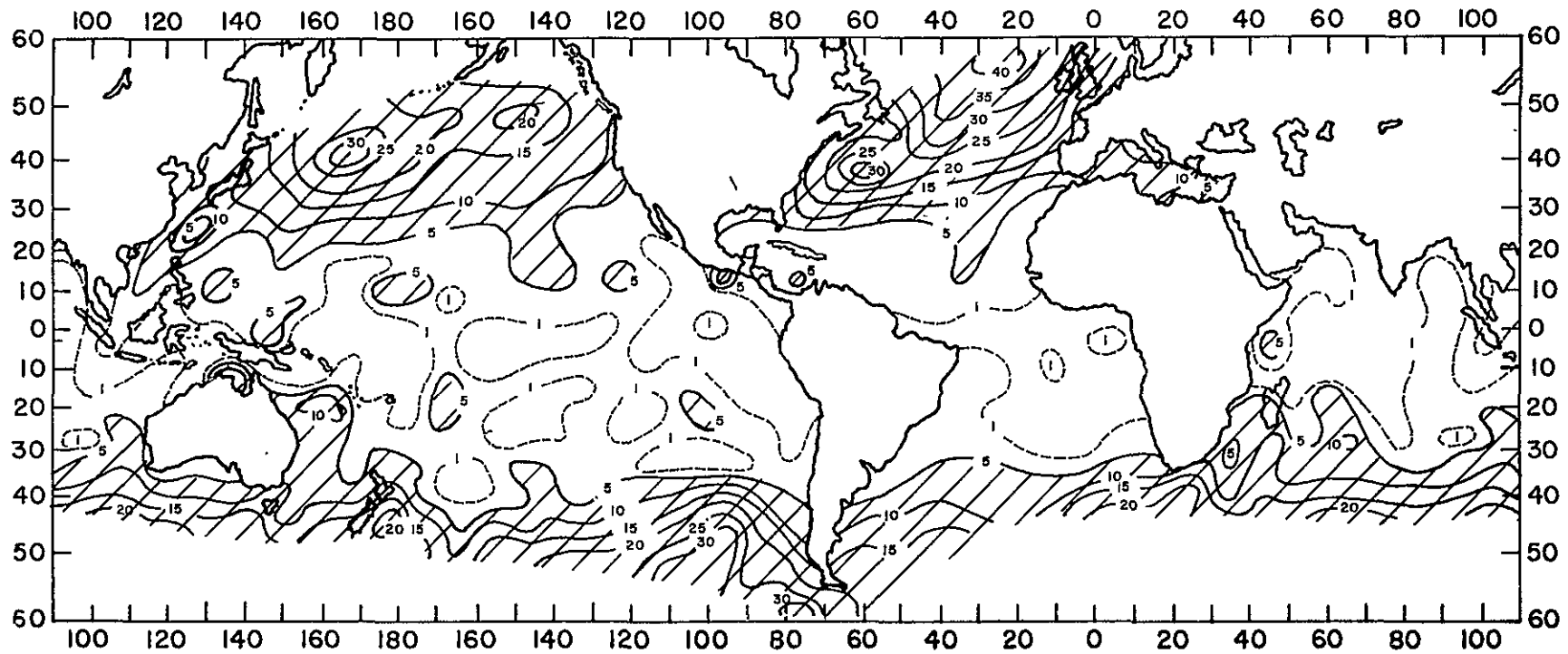

Figure 20. Frequency of Beaufort force 7 (15.5 m s^{-1}) or higher winds at Greenwich noon. (After McDonald, 1938).

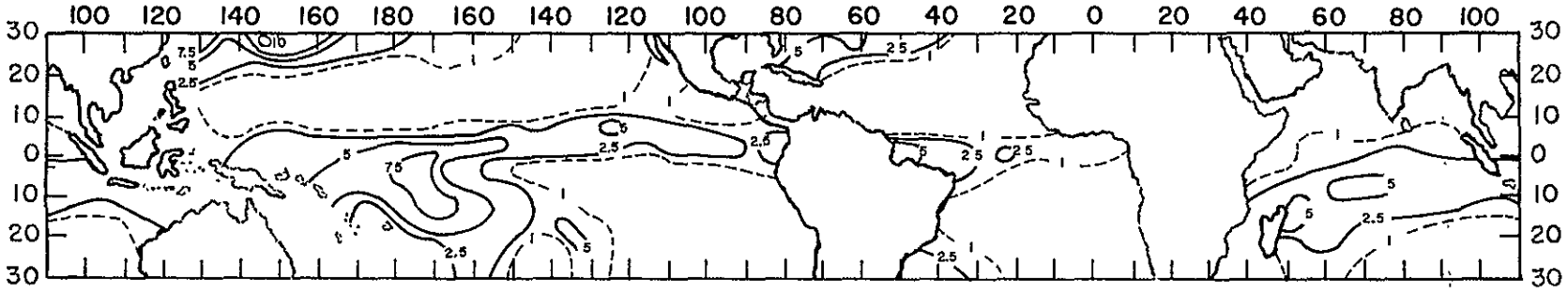

Figure 21. Frequency of light precipitation for the season December 1972 through February 1973. (The noon and midnight frequencies have been averaged).

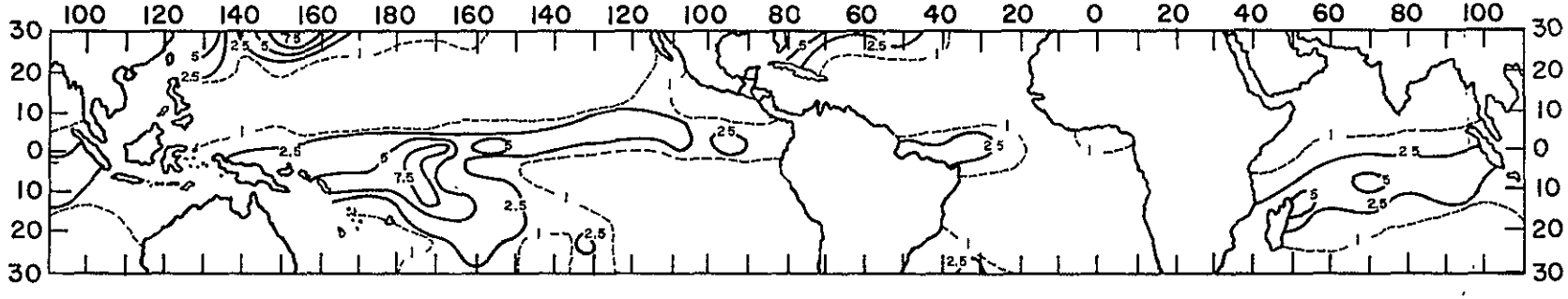

Figure 22. Frequency of moderate precipitation for the season December 1972 through February 1973. (The noon and midnight frequencies have been averaged).

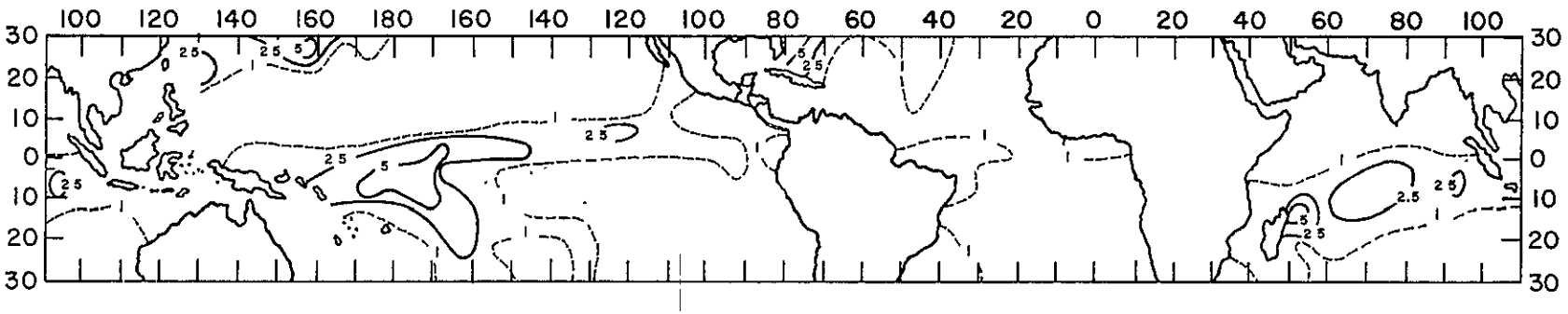

Figure 23. Frequency of heavy precipitation for the season December 1972 through February 1973. (The noon and midnight frequencies have been averaged).

contours in these three figures follow those in Figure 15, indicating that in the tropics the fraction of rainfall occurrences in the light, moderate, and heavy categories does not vary much from place to place; thus precipitation amount is proportional to precipitation frequency.

4.2 Day-Night Variation

One of the most interesting problems in oceanic precipitation research is the determination of its diurnal variation which, if it were known, would provide important information about the operation of the troposphere. Although the technique for precipitation determination used in this study is experimental, and although the data are available at only two local times (1130 and 2330), some insight into the diurnal variation of oceanic precipitation frequency can be gained. Figures 24 and 25 show the frequencies of noon and midnight precipitation (using the 0.25 mm hr^{-1} thresholds). The similarity in the two figures indicates that there is no large difference in the frequencies of noon and midnight precipitation. Table 5 shows the ratio of the noon precipitation frequency (D) to the sum of D and the midnight precipitation frequency (N) for both dry and wet oceanic regions between $20^{o}N$ and $30^{o}S$. The generally small difference between noon and midnight precipitation frequency is consistent with the results of Lavoie (1963) and Jacobson and Gray (1976) who analyzed precipitation data from small tropical islands and found an early morning maximum, a late afternoon minimum and little difference between noon and midnight. It is interesting, however, that in both wet and dry regions, higher rainfall rates tend to occur more often near local noon than near local midnight.

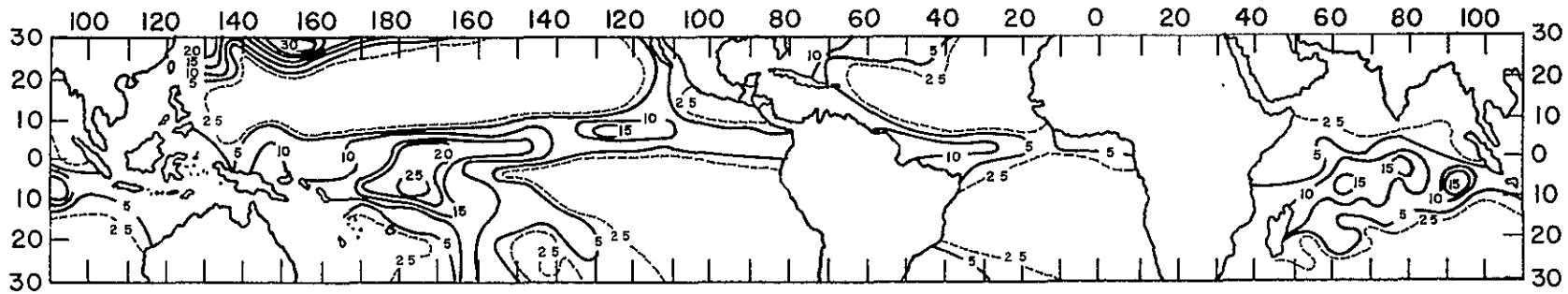

Figure 24. Frequency of precipitation near local noon for the season December 1972 through February 1973.

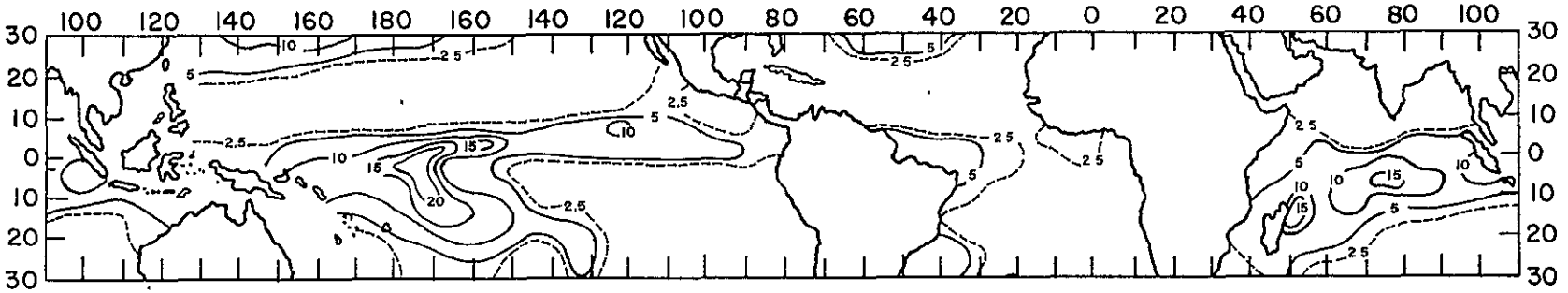

Figure 25. Frequency of precipitation near local midnight for the season December 1972 through February 1973.

TABLE 5

Fraction of the Total of Noon and Midnight Precipitation Events Occuring near Local Noon in Oceanic Regions Between $20^{o}N$ and $30^{o}S$

	$\frac{D}{D+N}$ (%)		
Rainfall Category	Dry Regions (0-5%)*	Wet Regions (5-100%)*	All Regions (0-100%)*
Light Rain	47	50	48
Moderate Rain	48	52	49
Heavy Rain	49	54	51
Very Heavy Rain**	53	61	57
All rain	49	52	50

* Precipitation frequencies

** Defined by the 5.0 mm hr^{-1} threshold temperatures in Table 4

5.0 SUMMARY AND CONCLUSIONS

Tropical oceanic precipitation frequencies have been obtained from Electrically Scanning Microwave Radiometer Data with the use of theoretical threshold brightness temperatures. The generally good agreement between the results of this study and both climatological precipitation frequency and frequencies of highly reflective clouds from concurrent visible satellite data indicate that passive microwave radiometry from satellites can be a valuable tool in the determination of oceanic precipitation.

For the period 22 December 1972 through February 1973 it was found that:

1. Tropical oceanic precipitation is organized into rather narrow convergence zones near the equator. The subtropical and eastern oceans are relatively dry.

2. The difference between local noon and local midnight precipitation frequencies is small, but heavier rainfall rates tend to occur more frequently near local noon.

3. The ratios of light, moderate, and heavy precipitation frequencies seem to vary only slightly throughout tropical oceanic regions.

REFERENCES

Battan, L. J., 1973: Radar Observation of the Atmosphere. University of Chicago Press, Chicago, pp. 64-83.

Chandrasekhar, S., 1960: Radiative Transfer. Dover Publications, Inc., New York, 393 pp.

Crutcher, H. L., and O. M. Davis, 1969: U.S. Navy Marine Climatic Atlas of the World, Vol. 8. NAVAIR 50-1C-54, Naval Weather Service Command, Washington D.C., chart 137.

Deirmendjian, D., 1963: Complete Microwave Scattering and Extinction Properties of Polydispersed Cloud and Rain Elements. Rand Corporation Report 12-422-PR, Santa Monica, California, 54 pp.

Dittberner, G. J., and T. H. Vonder Haar, 1973: Large-scale precipitation estimates using satellite data; application to the Indian monsoon. Arch. Met. Geoph. Biokl., Ser. B, 21, 317-334.

Fletcher, N., 1963: The Physics of Rainclouds, Cambridge University Press, Cambridge, 390 pp.

Herzberg, G., 1950: Molecular Spectra and Molecular Structure, I. Spectra of Diatomic Molecules, Second Edition. D. Van Nostrand Co., Princeton, N. J.

Holloway, J. L. Jr. and S. Manabe, 1971: Simulation of climate by a global general circulation model. I. Hydrological cycle and heat balance. Monthly Weather Review, 99, pp. 335-370.

Jackson, J. P., 1962: Classical Electrodynamics. John Wiley and Sons, New York, pp. 216-220.

Jacobs, W. C., 1968: The seasonal apportionment of precipitation over the ocean. Association of American Geographers Yearbook, V. 30, pp. 63-78.

Jacobson, R. W., and W. M. Gray, 1976: Diurnal Variation of Oceanic Deep Cumulus Convection. Colorado State University, Atmospheric Science Paper no. 243, Fort Collins, Colorado.

Lavoie, R. L., 1963: Some Aspects of the Meteorology of the Tropical Pacific Viewed from an Attol. Hawaii Institute of Geophysics Report no. 27.

Martin, D. W. and W. D. Scherer, 1973: Review of satellite rainfall estimation methods. Bull. Amer. Meteorol. Soc., 54, 7, 661-674.

Mc Donald, W. F., 1938: Atlas of Climatic Charts of the Oceans. U.S. Dept. of Agriculture, Weather Bureau, Washington, D.C.

Nordberg, W., J. Conaway, D. B. Ross and T. Wilheit, 1971: Measurements of microwave emission from a foam-covered, wind-driven sea. J. Atmos. Sci., 28, 429-435.

Oort, A. H., and E. M. Rasmusson, 1971: Atmospheric Circulation Statistics. NOAA Professional Paper 5, U.S. Dept. of Commerce, Rockville, MD, 323 pp.

Ramage, C. S., 1975: Preliminary discussion of the meteorology of the 1972-73 El Nino. Bull. Amer. Meteor. Soc., 56, 234-242.

Sellers, W. D., 1965: Physical Climatology. Univ. of Chicago Press, Chicago, 272 pp.

Shifrin, K. S., Yu. I. Rabinovich and G. G. Shchukin, 1968: Microwave radiation field in the atmosphere. In Transfer of Microwave Radiation in the Atmosphere, Trudy no. 222, A. I. Voeikov Main Geophysical Obsdrvatory, Leningrad.

Staelin, D. E., 1969: Passive remote sensing at microwave wavelengths. Proc. IEEE, 57, 427-439.

Taylor, R. C., 1973: An Atlas of Pacific Islands Rainfall, Hawaii Institute of Geophysics Data Report no. 25, University of Hawaii, Honolulu, Hawaii.

Taljaard, J. J., H. van Loon, H. L. Crutcher and R. L. Jenne, 1969: Climate of the Upper Atmosphere, Part 1 - Southern Hemisphere, vol. 1, National Center for Atmospheric Research, National Weather Records Center, and Dept. of Defense, Washington, D.C.

The Nimbus 5 Data Catalog, 1973: Volume 1 and 2, NASA/Goddard Space Flight Center, Greenbelt, MD.

Tolbert, C. W., A. W. Straiton, J. H. Douglas, 1958: Electrical Engineering Laboratory Report no. 104, University of Texas, Austin, TX.

Tucker, G. B., 1961: Precipitation over the North Atlantic Ocean. Quart. J. Royal Meteorol. Soc., 87, pp. 147-158.

Van Vleck, J. H., 1947: Absorption of microwaves by water vapor. Phys. Rev., 71, 425-433.

Westwater, E. R., 1972: Microwave Emission from Clouds. NOAA Technical Report ERL 219-WPL 18, NOAA/Environmental Research Laboratories, Boulder, CO. 66 pp.

Wilheit, T. T., 1972: The Electrically Scanning Microwave Radiometer (ESMR) Experiment, in The Nimbus-5 User's Guide, NASA/Goddard Space Flight Center, Greenbelt, MD, pp. 59-105.

Wilheit, T. T., 1975: The Electrically Scanning Microwave Radiometer (ESMR) Experiment, in The Nimbus 6 User's Guide, NASA/Goddard Space Flight Center, Greenbelt, MD., pp. 87-108.

Wilheit, T. T., M.S.V. Rao, T. C. Chang, E. B. Rodgers and J. S. Theon, 1975: The Remote Sensing of Rainfall Rates over the Oceans. Presented at the Second Conference on Atmospheric Radiation of the American Meteorological Society, Arlington, VA., October 29, 1975.

APPENDIX I

EMITTANCE OF A PLANE WATER SURFACE

Jackson (1962) calculates the amplitude of a plane electomagnetic wave which has been reflected from the interface between two dielectrics. His argument is easily extended to the case where the lower dielectric has a complex dielectric constant (a lossy dielectric). Suppose that the upper and lower dielectrics have permeabilities μ and μ' and dielectric constants κ and κ', respectively. The indicies of refraction are then

$$n = \sqrt{\mu\kappa} \qquad \text{(assumed to be real)} \tag{A1}$$

$$n' = \sqrt{\mu'\kappa'} = \gamma - j\lambda \tag{A2}$$

A useful quantity may be defined as

$$n_s^2 = \tfrac{1}{2}\left[\gamma^2 - \lambda^2 + n^2\sin^2 i + \sqrt{(\gamma^2-\lambda^2-n^2\sin^2 i)^2 + 4\gamma^2\lambda^2}\,\right] \tag{A3}$$

where i is the angle of incidence (measured from the normal to the interface).

Snell's Law becomes

$$\frac{\sin r}{\sin i} = \frac{n}{n_s} \tag{A4}$$

where r is the angle of refraction.

If E_0 is the amplitude of the electric field in the incident wave, E_0' that for the refracted wave (at the surface of the lossy dielectric), and E_0'' that of the reflected wave, we have for horizontally polarized radiation,

$$P \equiv \frac{\mu}{\mu'}\left(\frac{\tan i}{\tan r} + j\frac{\gamma\lambda}{nn_s}\sec i \sec r\right) \tag{A5}$$

$$\frac{E_o'}{E_o} = \frac{2}{1+P} \tag{A6}$$

$$\frac{E_o''}{E_o} = \frac{1-P}{1+P} \tag{A7}$$

For vertically polarized radiation,

$$q \equiv \frac{\mu}{\mu'}\left(\sin 2i + 2j\frac{\gamma\lambda}{nn_s}\sin r \cos i\right) \tag{A8}$$

$$\frac{E_{o'}}{E_o} = \frac{n}{n_s} \cdot \frac{2\sin 2i}{\sin 2r+q} \tag{A9}$$

$$\frac{E_o''}{E_o} = \frac{q-\sin 2r}{q+\sin 2r} \tag{A10}$$

For normal incidence (i=o), both polarizations reduce to

$$\frac{E_o'}{E_o} = \frac{2n}{n'+n} \tag{A11}$$

$$\frac{E_o''}{E_o} = \frac{n'-n}{n'+n} \tag{A12}$$

The emittance is given by

$$\varepsilon = 1 - \left|\frac{E_o''}{E_o}\right|^2 \tag{A13}$$

The above applies to any plane surface; one simply needs to use the appropriate permeabilities and dielectric constants. For water, Westwater (1972) gives

$$\kappa = \kappa_\infty + \frac{\kappa_o - \kappa_\infty}{1+\left(\frac{j\lambda_s}{\lambda}\right)^{1-\Omega}} \qquad \text{(A14)}$$

where

$$\kappa_\infty = 4.5$$

$$\kappa_o = \frac{32155.45}{T} - 29.62 \qquad \text{(A15)}$$

$$\log_{10}\lambda_s = \frac{921.0935}{T} - 2.9014 \qquad \text{(A16)}$$

and $\Omega = 0.02$

T is expressed in Kelvin, and λ in centimeters. Using (A14) in (A13) and assuming that

$$\kappa_{air} = \mu_{air} = \mu_{water} = 1 \qquad \text{(A17)}$$

gives the values in Figures 4 and 5.

APPENDIX II

ESMR FLIGHT MODEL PARAMETERS
(After Wilheit, 1972)

Antenna	
Aperture Size (Linear Array Dimension)	83.3 cm (32.80 in.)
Aperture Size (Feed Array Dimension)	85.5 cm (33.66 in.)
Number of Linear Elements	103
Number of Slots per Element	81
Amplitude Distribution (Linear Array)	-40 db sidelobe Taylor distribution
Amplitude Distribution (Feed Array)	-35 db sidelobe Taylor distribution
Broadside Half Power Beamwidth	1.4°
Number of Beam Positions	78
Antenna Beam Efficiency	90 to 92.7%
Beam Scan Angle	±50°
Antenna Loss	1.7 db
Beam Squint Angle	-3.2° nominal
Polarization	Linear (E vector parallel to flight direction)
Cross Polarization	-25 to -36 db
Failsafe Angle (Non-Scanning Mode)	-13.7°
VSWR	<1.15
Radiometer	
Center Frequency	19.35 GHz
Bandwidth IF (Nominal)	50 - 150 MHz
Bandwidth RF (Nominal)	300 MHz
Local Oscillator	19.35 GHz
Mixer Noise Figure	6.5 db -
ΔT_{rms}/47 ms	1.5°K
Absolute Accuracy	2°K
Dynamic Range	50 - 330°K
Calibration:	
Dicke Load	~338 ±0.1°K
Ambient Load	Local ambient
Sky Horn	<3°K